Master's Thesis

Load Adaptive Modulation to Heat Non-Ferromagnetic Material

Si-Hoon Jeong

Department of Electrical Engineering

Graduate School of UNIST

2019

Load Adaptive Modulation to Heat Non-Ferromagnetic Material

Si-Hoon Jeong

Department of Electrical Engineering

Graduate School of UNIST

Load Adaptive Modulation to Heat Non-Ferromagnetic Material

A thesis/dissertation
submitted to the Graduate School of UNIST
in partial fulfillment of the
requirements for the degree of
Master of Science

Si-Hoon Jeong

3 Dec. 2018

Approved by

Advisor

Jee-Hoon Jung

Load Adaptive Modulation to Heat Non-Ferromagnetic Material

Si-Hoon Jeong

This certifies that the thesis/dissertation of Si-Hoon Jeong is approved.

3 Dec. 2018

signature

Advisor: Jee-Hoon Jung

signature

Katherine Ann Kim

signature

Gang-Il Byun

Abstract

Induction heating (IH) cooktops are popular to heat various vessels fast and safely in the kitchen. Conventional IH cooktop system have been developed to heat the vessel of ferromagnetic materials. Because the vessel of non-ferromagnetic materials has low-resistance which induces large resonant current to power switches in series resonant IH inverters. Hence, the rated power cannot be transferred to the vessel due to overcurrent which is higher the rated switch current. In this thesis, a load adaptive modulation (LAM) method is proposed to heat the vessel of non-ferromagnetic and ferromagnetic materials in a single IH burner. The LAM can change the magnitude of the input voltage of the IH working coil and the operating frequency induced to the IH working coil according to the resistance of the vessel. The operational principle and the design method are analyzed to implement the proposed LAM and its power control. The validity of the design method and the control algorithm is experimentally verified using a 2 kW prototype series resonant full-bridge inverter with the IH working coil.

Contents

List of Figures

List of Tables

List of Abbreviations

IH	Induction Heating
LAM	LAM
HFO	HFO
THM	THM
SRC	SRC
PFC	Power Factor Correction
PFM	Pulse Frequency Modulation
ZVS	Zero Voltage Switching
DSP	Digital Signal Processor
EMI	Electromagnetic Interference
MOSFET	Metal-Oxide-Semiconductor Field-Effect Transistor
SiC	Silicon Carbide

I. Introduction

The traditional concept of gas stove is the most popular in the market. In recent years, induction cooktop has become increasingly popular. Induction cooktop not only offers a faster heating performance compared to the traditional solutions (Gas and electric stoves), but also offers cleanness, safety and high efficiency [1-3]. Some of these advantages derive from the fact that the heating is directly generated in the vessel, unlike the traditional contact-heating solutions. For this reason, the high efficiency of the induction cooktop has been paid attention of researchers devoted to highly efficient power electronic systems. The principle of induction heating is to create a high frequency current which induce a magnetic flux. This magnetic flux produces eddy current which induce joule heating into the vessel. The generated heat is due to the eddy currents induced in the bottom layer of vessel combined with the hysteresis losses from the vessel.

The conceptual diagram of the conventional induction cooktop is shown in Fig. 1. The conventional induction cooktop has a diode rectifier, a resonant network connected in series, a bridge circuit and a working coil. The half-bridge SRC is used due to its simple structure and its cost-effectiveness. The planar type IH working coil and the vessel is approximated by a transformer model [4-6]. Fig. 2 shows the transformer model as a load model of induction cooktop. The equivalent load resistance consists of the IH working coil and the series connected resistance of vessel. Therefore, the primary-side switch current is inversely proportional to the resistance of the vessel. For this reason, the conventional induction cooktop has been developed to heat the ferromagnetic materials which have high resistance to reduce the primary switch current. The high resistance material is mostly a ferromagnetic material which have high permeability and resistivity. The ferromagnetic material has low skin-depth which is induced by high resistivity and permeability. However, the vessel made of the non-ferromagnetic materials such as aluminum and copper induce the high primary switch current in induction cooktop and fail to deliver proper transfer power to the vessel due to overcurrent protection (OVP). This becomes a problem in that a significant portion of the vessels on the market are currently made of aluminum and copper as it offers low manufacturing cost. The heating capability for various materials is the most important to improve the functionality and the usability of the induction cooktop.

To overcome this problem, the very few non-ferromagnetic material-compatible induction cooktops called all-metal IH are proposed on the market. A common concept for all-metal IH technology is to increase the operating frequency applied into the IH working coil [7-9]. It is based on the skin-depth effect. Skin depth is normally expressed as $\delta = 1/\sqrt{f\pi\mu\sigma}$, where f is the operating frequency, μ is the permeability of the conducting material, σ is the conductivity of the conducting material. Therefore, when the operating frequency applied to the IH working coil increases, skin depth decreases and a high equivalent load resistance is obtained to reduce the primary switch current.

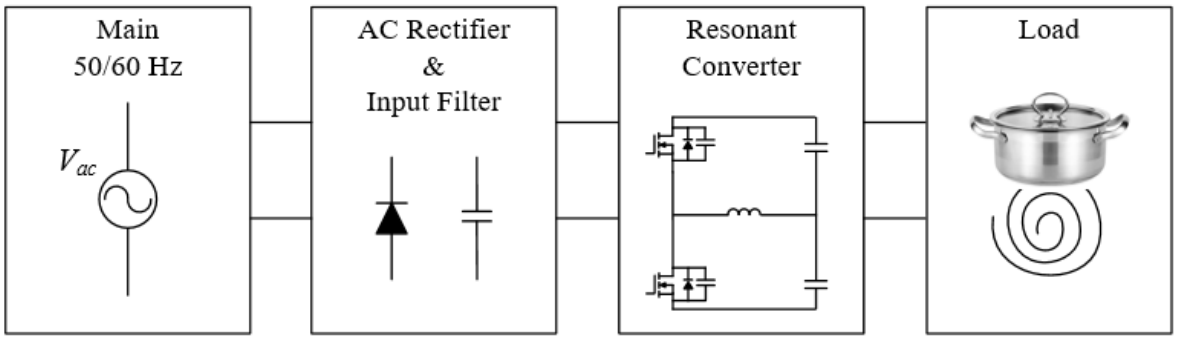

Fig. 1. Concept block diagram of induction cooktop

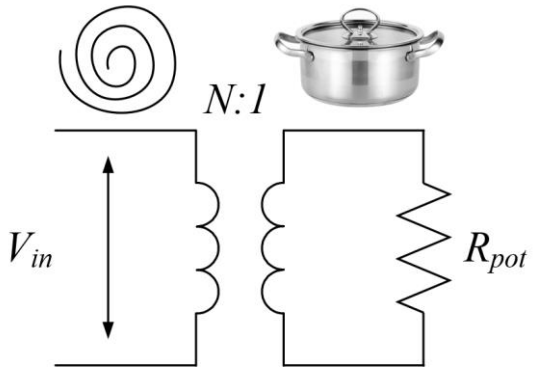

Fig. 2. Equivalent load model of an induction cooktop

As part of this method, the THM method is proposed [10]. In THM method, the operating frequency induced to the IH coil is three times higher the switching frequency by designing resonant network which have the tripled resonant frequency compared with the switching frequency [11-12]. Fig. 3 shows experimental results of THM. Fig. 4 shows circuit of THM resonant inverter. In the THM method, resonant network is designed at the resonant frequency which is three times higher the switching frequency. Therefore, the voltage gain of the resonant network is reduced to about 1/3 by removing other harmonic components. Although the load equivalent load resistance is sufficiently high, active PFC is needed to compensate for the lowered voltage gain. THM method not only increases the unit cost of the product, it is also an inefficient method.

Another all-metal IH technology is a HFO method [13]. It simply increases the equivalent load resistance by increasing the switching frequency to 100 kHz. Therefore, it causes the low Power efficiency due to high switching losses. To compensate this demerit, SiC devices is adopted in the HFO method. The SiC metal oxide semiconductor field effect transistor (MOSFET) has low on-resistance, high-breakdown voltage compared to MOSFET and high heat conductivity. SiC MOSFET dramatically decrease the switching losses. However, the unit cost increases. In addition, since the area of the package must be widened to cool the heat of the high frequency

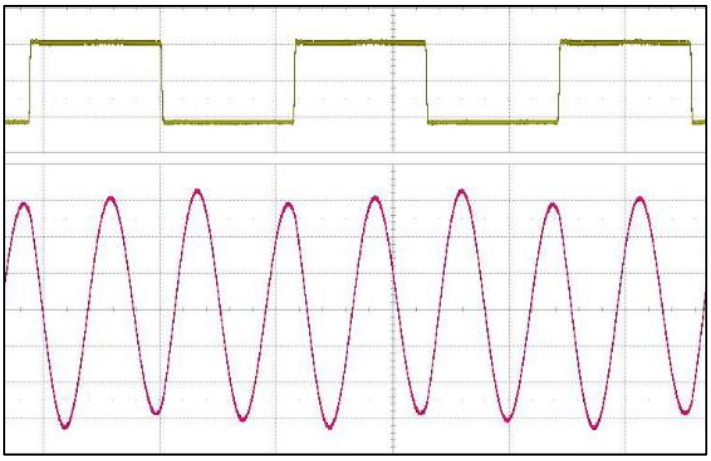

Fig. 3. Experimental results of THM

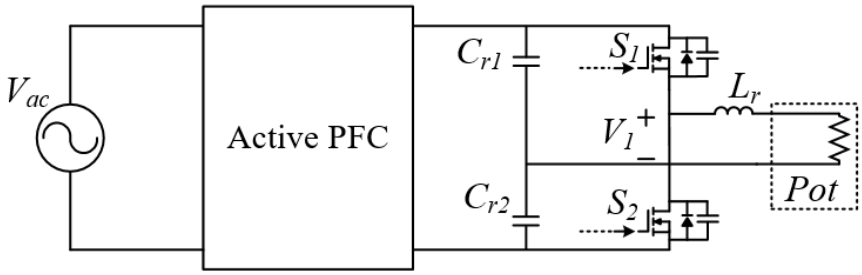

Fig. 4. Circuit of THM resonant inverter

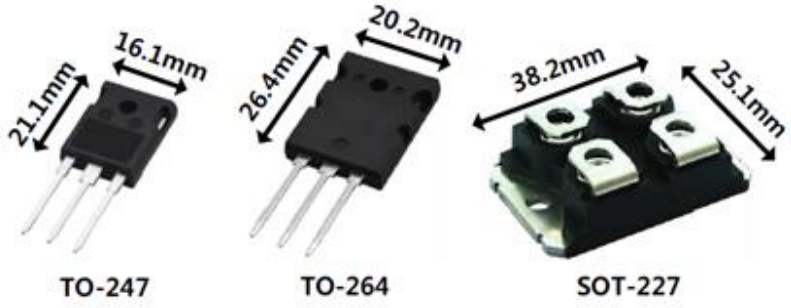

Fig. 5. Switching device according to package type

switching operation. Therefore, thermal analysis is required to select the package type for SiC device. It is necessary to analyze the loss by calculating the thermal resistance of the insulating pater and the thermal grease considering the area contacted with the heat sink according to SiC MOSFET package type [14]. Fig. 5 shows switching device according to package type. To cool the heat generated by high-frequency switching of the SiC, a switch package having a large heat-contact area such as SOT-227 shown in the figure 5 should be selected. The selected device SOT-227 package has higher unit costs than typical TO-247 or TO-264 packages. Therefore, the all-metal IH technology proposed to date has a disadvantage of high cost.

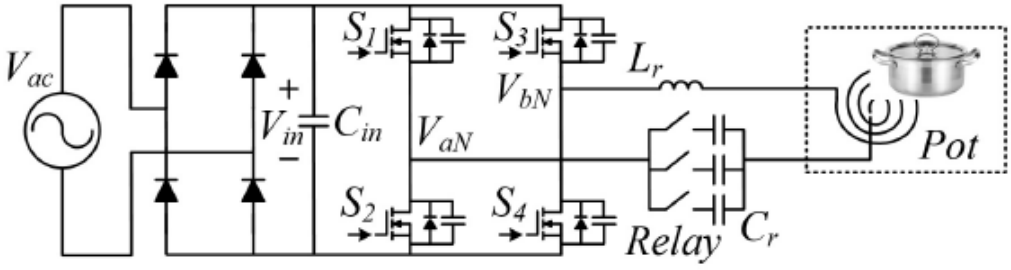

Fig. 6. Circuit diagram of LAM IH inverter

In this thesis, the LAM which implements all-metal IH technology in a full-bridge structure using MOSFET is proposed. Fig. 6 shows Circuit diagram of LAM IH inverter. The LAM has four modulation modes which can control the input voltage and the operating frequency induced the IH working coil. The various modulation modes can properly control the magnitude of the primary switch current according to the material of vessel. The inverter which implements proposed method has no input voltage drop because it not uses the high order operation. Therefore, PFC circuit is not necessary for LAM to boost up the effective input voltage, which will be cost-effective and will improve power density. The operational principles and the practical design methodology will be briefly introduced in Section 4.1. Also, the proposed algorithm is analyzed in Section 4.2. In Section 4.3, the proposed control algorithm will be verified by using simulation and experimental results. Finally, the conclusion, the summary, and the future plan of this thesis will be presented in last three chapters.

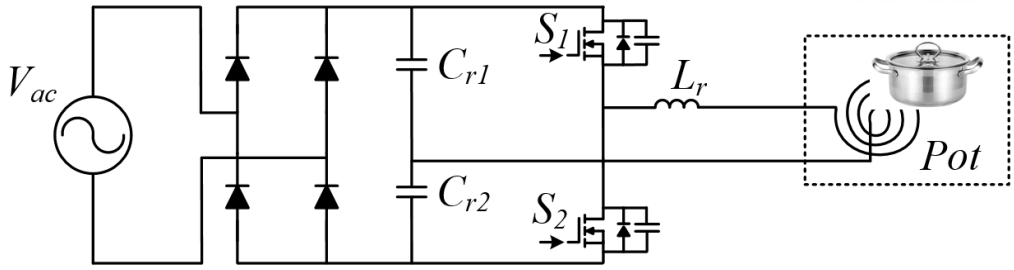

Fig. 7. Circuit diagram of half bridge SRC

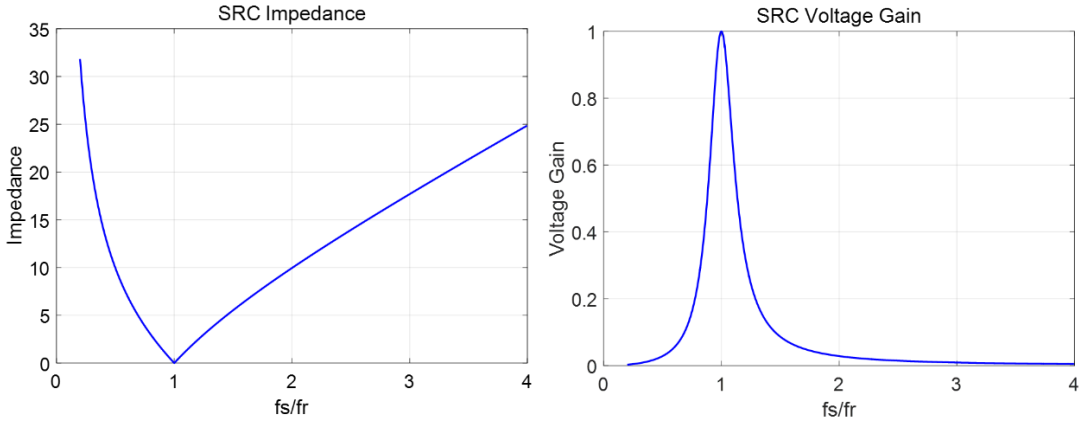

Fig. 8. Voltage gain and impedance characteristics of SRC (SRC)

II. Theoretical analysis of series resonant inverter for induction cooktop

In the IH converter, a SRC is widely used. The resonant converter improves efficiency by generating sinusoidal switching waveforms instead of the commonly used square waveforms. The sinusoidal waveform offers that the total harmonic distortion and electromagnetic interference (EMI) will be reduced. And the resonant converter enables the Zero Voltage Switching (ZVS). With ZVS operation, the switch in the resonant converter is turned on when the voltage across it is zero, thus switching losses are minimized [15-20].

Fig. 7 shows circuit diagram of the half-bridge SRC (SRC). SRC has a series L-C resonant network serving as a major part in power conversion process. The resonant network consists of a resonant capacitor C_r and a resonant inductor L_r connected in series. The equivalent load resistance which is the equivalent load resistance of vessel in IH converter is in series with the resonant network and impedance of the resonant network Z_r is a function of the resonant frequency and switching frequency. Detailed theoretical analysis of the SRC is described in Section 2.1. and Section 2.2. Fig. 8 shows the voltage gain and impedance characteristics of SRC. At resonant frequency $f_r = 1/(2\pi\sqrt{L_r C_r})$, the impedance of the resonant network reaches its minimum ($Z_r = 0$). Therefore, the voltage gain of the resonant network reaches its maximum ($G_v = 1$). The SRC can control the voltage gain of the resonant network

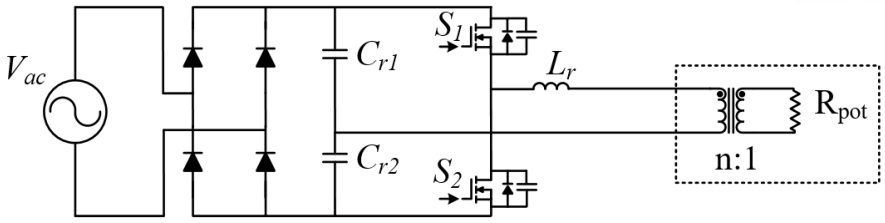

Fig. 9. Simplified circuit model of SRC for induction cooktop

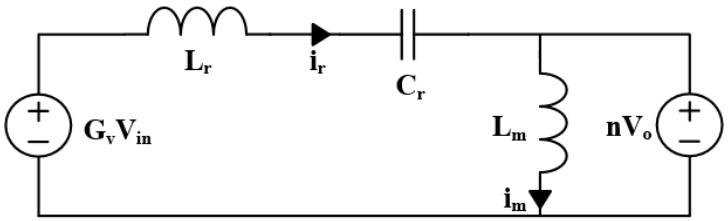

Fig. 10. Equivalent circuit of resonant network

by adjusting the normalized frequency ($f_n = f_r/f_s$) which is a function of the resonant frequency and the switching frequency ratio and can control the output power. In this section, the operational principle of SRC for induction cooktop is introduced briefly and the practical design methodology considering IH load characteristics.

2.1 Equivalent load resistance range for heating a desired power

The simplified circuit model of SRC for induction cooktop is shown in Fig.9. Fig. 9 is the circuit which is combined with Fig. 3 and Fig.6. The load model of the SRC for the induction cooktop is approximated by a transformer model which consist of the IH working coil on the primary side and the vessel on the secondary side. Fig. 10. shows equivalent circuit of resonant network. It has the input voltage, the equivalent load resistance in primary side, and the resonant network which is two combinations of the resonant inductance and the resonant capacitor. This model is used to derive the load characteristics, the resonant network voltage gain, and resonant current. The derived equations are expressed by the transfer power and switch current which is used to design SRC for induction cooktop. The SRC for induction cooktop is designed to meet the two requirements which are the selected switch rated current and the desired transmission power.

The transmission power of the induction cooktop is determined by the equivalent load resistance and the voltage induced to the IH working coil. The transmission power equation is described as follows:

$$P_{transfer} = \frac{V_{coil}^2}{R_{eq}} \quad (1)$$

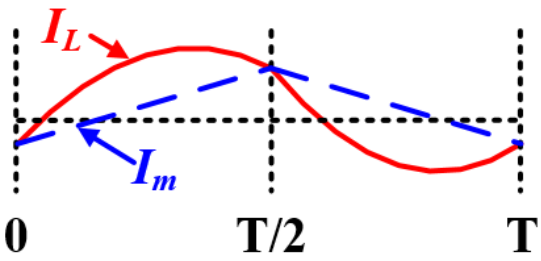

Fig. 11. Resonant network current waveform at resonant frequency.

where $P_{transfer}$ is transmission power, V_{coil} is the voltage induced to the IH working coil in primary, R_{eq} is the equivalent load resistance. The voltage induced to the IH working coil in primary and the equivalent load resistance are described as follows:

$$V_{coil} = \frac{\sqrt{2}}{\pi} G_v V_{in} \tag{2}$$

$$R_{eq} = n^2 R_{container} \tag{3}$$

where G_v is the resonant network voltage gain, V_{in} is the input voltage, n is the number of turns in primary, R_{vessel} is the resistance of the vessel. Therefore, the transmission power of the SRC for induction cooktop is determined by the equivalent load resistance when the input voltage is regarded as a fixed value. As the equivalent load resistance decreases, the transmission power increases. The resonant network voltage gain derived in [21] is described as follows:

$$G_v = \frac{V_{out}}{V_{in}} = \frac{n}{2} \cdot \frac{1}{1 + j \cdot \frac{\pi^2}{8} \cdot Q \cdot (\frac{\omega_s}{\omega_r} - \frac{\omega_r}{\omega_s})} \tag{4}$$

where $\omega_r = 2\pi f_r$, $\omega_s = 2\pi f_s$. The voltage gain of SRC for induction cooktop is controlled by adjusting switching frequency.

In the SRC for induction cooktop, the primary side switch current is a factor in determining the rated current of the switch. The current flowing through the resonant network is approximated by the primary side current. Fig. 10 shows the equivalent circuit of the resonant network at resonant frequency and Fig. 11 shows the waveform of the resonant network current at resonant frequency. The peak current of the magnetizing inductance and the resonant network current at the resonant frequency are derived as follows:

$$I_m = \frac{4nV_{container}}{L_m T_s} \tag{4}$$

$$I_r = \sqrt{2} I_{rms} \sin(2\pi f_r + \phi) \tag{5}$$

where L_m is magnetizing inductance, L_r is the resonant inductance, T_s is the switching period, I_{rms} is the

RMS current of the resonant network. There is a point where the resonant network current and the magnetizing inductor current are the same at each half-cycle according to the current waveform in Fig. 11. Thus, (6) is derived as follows:

$$\sqrt{2}I_{rms}\sin(\phi)=\frac{4nV_{pot}}{L_mT_s} \tag{6}$$

where V_{vessel} is the voltage induced to the vessel. The difference between the resonant network current and the magnetizing inductor current is equal to the current delivered to the vessel. Thus, (7) is derived as follows:

$$\int_0^{\frac{T_S}{2}}(i_r-i_m)dt=\frac{T_sV_{pot}}{2nR_{pot}} \tag{7}$$

The RMS current of the resonant network are the voltage induced to the vessel are derived by summarizing the above equations. Thus, (8) and (9) is derived as follows:

$$I_r=\frac{1}{8}\frac{V_{pot}}{nR_{pot}}\sqrt{\frac{2n^4R_{pot}^2T_s^2}{L_m^2}+8\pi^2} \tag{8}$$

$$V_{pot}=\frac{V_{coil}}{n} \tag{9}$$

Since the left terms in the root of equation (8) is a very small value, it can be approximated by equation (10). Equation (10) is derived as follows:

$$I_r=\frac{1}{8}\frac{V_{pot}}{nR_{pot}}\sqrt{8\pi^2}=\frac{\sqrt{2}\pi}{4}\frac{V_{pot}}{nR_{pot}} \tag{10}$$

Therefore, after determining a switch rated current, can determine the minimum value of the equivalent load resistance which does not exceed the switch rated current. And, the maximum equivalent load resistance value can be determined by substituting the minimum transmission power into equation (1). When the maximum equivalent load resistance and the minimum equivalent load resistance are determined, the equivalent load resistance range is determined. Therefore, when the equivalent load resistance value measured on the primary side is within this equivalent load resistance range, it can be heated to the desired power in an operation that does not exceed the switch rated current.

2.2 Operational principle

In this section, the operational principles of the conventional SRC for induction cooktop is analyzed. There are two modulation modes based on the resonant current, which are the powering and the freewheeling process, respectively. The power is transferred from the primary side to the vessel when

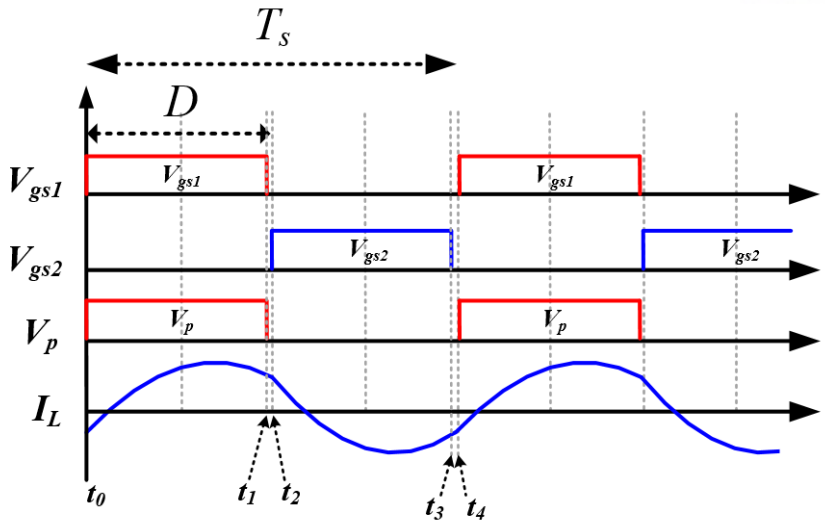

Fig. 12. Operational waveforms of SRC for induction cooktop

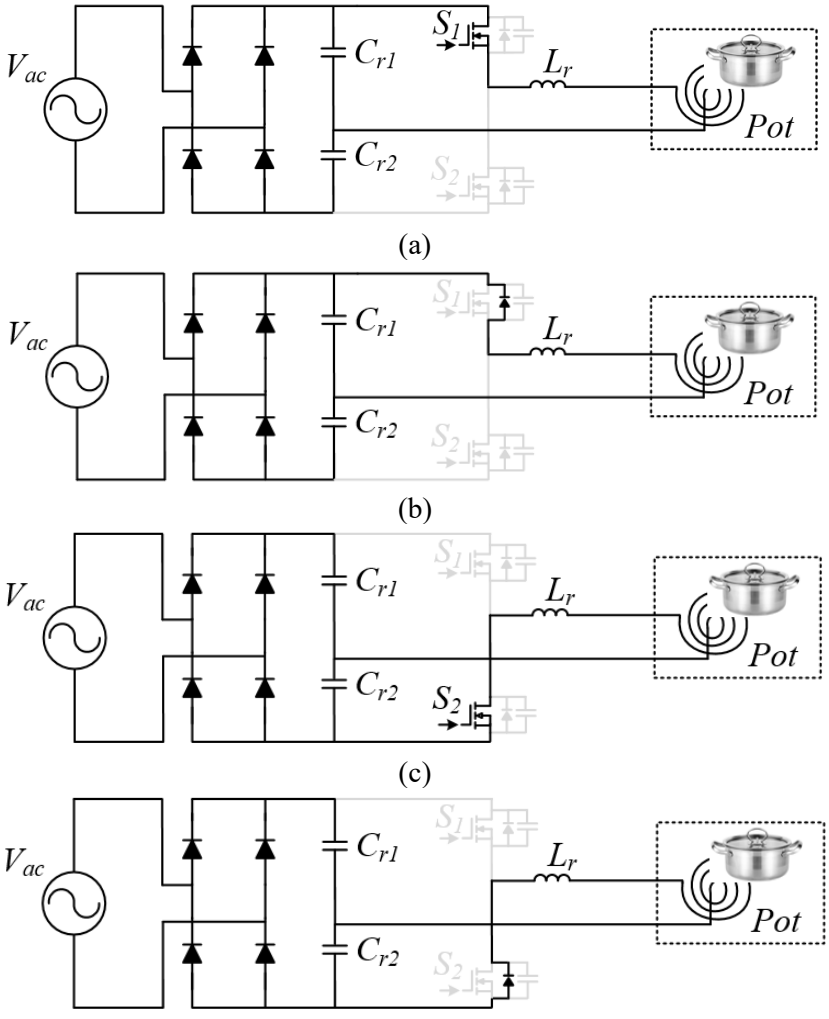

Fig. 13. Operational circuit diagram of SRC for induction heating

the high side switch is turn on. Fig. 13 Shows the operational circuit diagrams of SRC for induction cooktop. Fig. 13(a) and (c) show the operational circuit diagrams of the powering mode. In the freewheeling process, the power is not transferred to the vessel and magnetizing current is sum of the output current referred to as the primary side. Fig. 13(b)(d) is the operational circuit diagram of the freewheeling mode.

Mode 1:(t_0-t_1) [Fig. 13(a)]: The higher switch S_1 is turn-on at t_0. This mode is powering mode which transfer the power to the vessel. The resonant current I_L flows through S1. The current direction of Switch S1 is negative direction. It guarantees zero voltage of switch S1. The zero-voltage switch (ZVS) of switch S1 is achieved at t_0.

Mode 2:(t_1-t_2) [Fig. 13(b)]: The higher switch S1 is turn-off at t_1. The resonant current IL charges the output capacitance of the higher switch S1 and discharges the output capacitance of the lower switch S2 during the turn-off transient period of S1. After the output capacitance of the lower switch S2 is fully discharged, the body diode of S2 is conducted before t_2.

Mode 3:(t_2-t_3) [Fig. 13(c)]: The lower switch S2 is turn-on at t_2. This mode is similar to the powering mod of mode 1. The current direction of switch S2 is positive direction. The zero-voltage switch (ZVS) of switch S2 is achieved at t_3.

Mode 4:(t_3-t_4) [Fig. 13(d)]: The lower switch S2 is turn-off at t_3. The resonant current IL charges the output capacitance of the lower switch S2 and discharges the output capacitance of the higher switch S1. After the output capacitance of the higher switch S1 is fully discharged, the body diode of S1 is conducted before t4. At the mode 1, the ZVS is achieved by repeating this procedure.

2.3 Characteristics of the IH cooktop according to material of vessel

In this section, the load characteristics of the SRC for induction cooktop is analyzed and introduce the design considerations and challenge for the induction cooktop converter. As described in the previous section, the load equivalent load resistance varies depending on the material of the vessel. Heating the low-resistivity materials which has the low equivalent load resistance is a challenge because the low equivalent load resistance induces the high switch current which increases the switch rated current. Fig. 14 shows the IH working coil with 16 turns which is used in induction cooktop product. Fig. 15 shows the examples of vessels according to materials. Fig. 16 shows the RMS switch current according to the material of the vessels. This figure is plotted by using equation (8). As shown in Fig.

Fig. 14. IH working coil with 16 turns

(a) (b) (c)

Fig. 15. Examples of vessels according to material:
(a) SUS-304 18-8, (b) SUS-304 18-10, (c) Aluminum

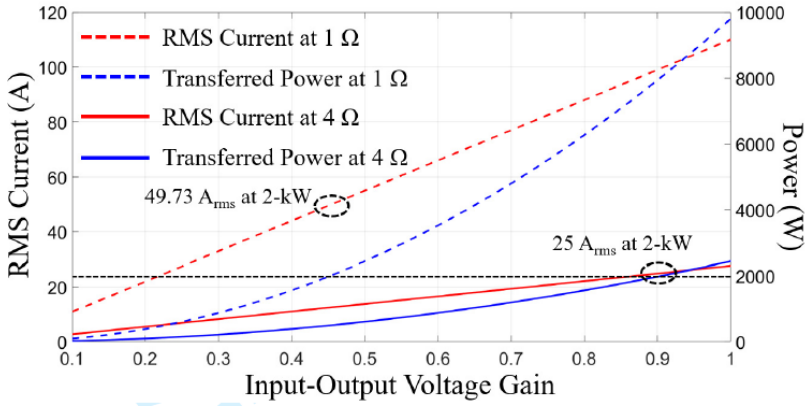

Fig. 16. RMS switch current according to resistance of vessel

16, the aluminum vessel which is the ferromagnetic material induces the higher RMS switch current than the other vessels based on 2 kW power condition. It causes a very high switch rated current under the condition of heating in the same burner. The way to overcome this problem is to increase the equivalent load resistance of the SRC for induction cooktop. The traditional ways to increase the equivalent load resistance of the IH converter are to increase the operating frequency induced to the IH

TABLE I SIMULATION DESIGN SPECIFICATION OF CONVENTIONAL IH SYSTEM

Transmission Power, P_o	2.0 kW	SUS-304 18-8 Resistance of vessel	2.1 Ω, at 24.7 kHz
Input Voltage, V_i	220 Vdc	SUS-304 18-8 Resistance of vessel	0.9 Ω, at 37.5 kHz
Turn numbers, N	16 turns	Aluminum Resistance of vessel	0.3 Ω, at 36.0 kHz
Resonant Inductance, L_r	28.2 uH	Resonant Frequency, f_r	21.8 kHz
Resonant Capacitance, C_r	1,880 uF	Switching Frequency, f_s	24.7 kHz
Resonant Inductance, L_r	15.1 uH	Resonant Frequency, f_r	29.8 kHz
Resonant Capacitance, C_r	1,880 uF	Switching Frequency, f_s	37.5 kHz
Resonant Inductance, L_r	14.7 uH	Resonant Frequency, f_r	30.2 kHz
Resonant Capacitance, C_r	1,880 uF	Switching Frequency, f_s	36.0 kHz

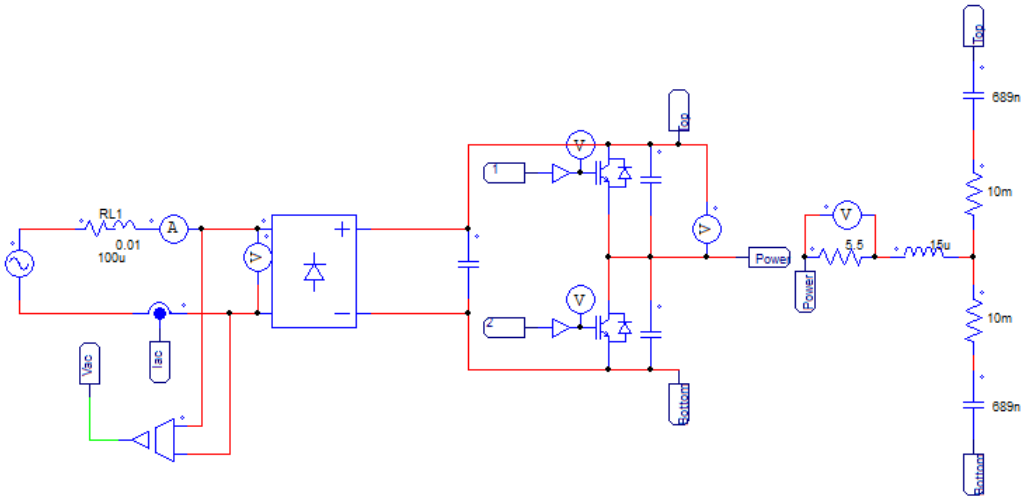

Fig. 17. Simulation model of conventional SRC for induction cooktop

working coil and increase the number of turns in primary. However, increasing the number of turns in primary has limitation due to the high coil conduction losses which is dominant to the total loss of the IH converter. Increasing the operating frequency induced to the IH working coil by increasing the switching frequency causes the high switching losses. Especially, the switching frequency must increase dramatically in order to heat the non-ferromagnetic material. Therefore, the conventional induction cooktops are not compatible with the non-ferromagnetic material.

2.4 Simulation & experimental results

In this section, the PSIM simulation and experimental results of the 3 kW rated conventional IH prototype inverter which consists of the half-bridge series resonant structure. The specification of the

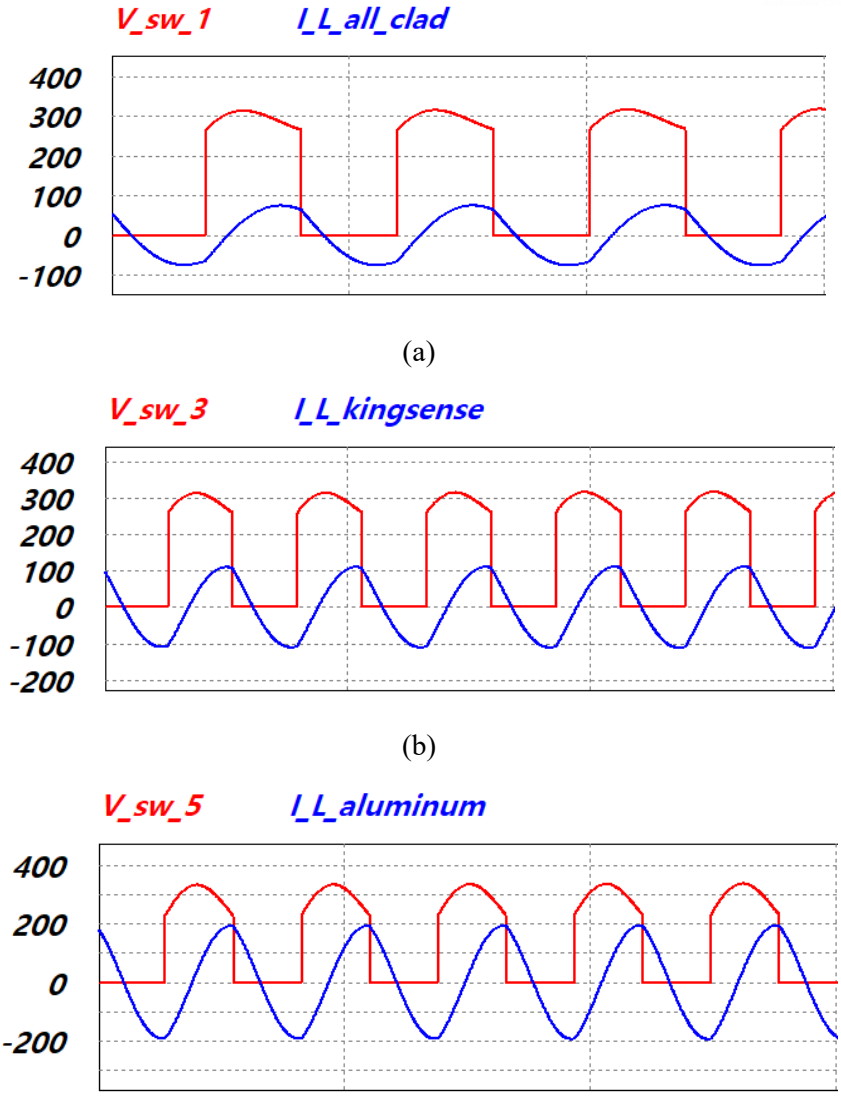

Fig. 18. Simulation waveforms of conventional SRC for induction cooktop: (a) SUS-304 18-8, (b) SUS-304 18-10, (c) Aluminum

simulation is shown in TABLE I. Fig. 17 shows simulation model of the conventional SRC for induction cooktop. The number of the coil turns in primary of IH working coil is 16 turns which is widely used for heating the ferromagnetic material in industry. The resonant inductance and capacitance are determined as the factors measured based on the coil which have 16 turns in primary. The materials of the vessel examples are STS-304 18-8, STS-304 18-10, and aluminum shown in Fig. 15. STS-304 18-8 material is commonly used as the ferromagnetic vessel which has high resistance. STS-304 18-10 material has the relatively low resistance compared to the STS-304 18-8 material. Aluminum material is used as the representative sample of common kitchen vessels. Fig. 18 shows the simulation waveforms according to the material of the vessel. TABLE II shows the simulation results according to the material of the vessel. The output power and switch current according to the material of the vessel

TABLE II SIMULATION RESULT OF CONVENTIONAL IH SYSTEM

SUS-304 18-8	Input Voltage, V_i	220 Vdc	Input Current, I_i (RMS)	13.50 A
	Transmission Power, P_o	2.97 kW	Switch current (RMS)	40.06 A
SUS-304 18-10	Input Voltage, V_i	220 Vdc	Input Current, I_i (RMS)	13.54 A
	Transmission Power, P_o	2.98 kW	Switch current (RMS)	59.07 A
Aluminum	Input Voltage, V_i	220 Vdc	Input Current, I_i (RMS)	13.63 A
	Transmission Power, P_o	3.0 kW	Switch current (RMS)	100.39 A

TABLE III EXPERIMENT DESIGN SPECIFICATION OF CONVENTIONAL IH SYSTEM

Transmission Power, P_o		3.0 kW	SUS-304 18-8 Resistance of vessel	2.1 Ω, at 24.7 kHz
Input Voltage, V_i		220 Vdc	SUS-304 18-8 Resistance of vessel	0.9 Ω, at 37.5 kHz
Turn numbers, N		16 turns	Aluminum Resistance of vessel	0.3 Ω, at 36.0 kHz
SUS-304 18-8	Resonant Inductance, L_r	28.2 uH	Resonant Frequency, f_r	21.8 kHz
	Resonant Capacitance, C_r	1,880 uF	Switching Frequency, f_s	24.7 kHz
SUS-304 18-10	Resonant Inductance, L_r	15.1 uH	Resonant Frequency, f_r	29.8 kHz
	Resonant Capacitance, C_r	1,880 uF	Switching Frequency, f_s	37.5 kHz
Aluminum	Resonant Inductance, L_r	14.7 uH	Resonant Frequency, f_r	30.2 kHz
	Resonant Capacitance, C_r	1,880 uF	Switching Frequency, f_s	36.0 kHz

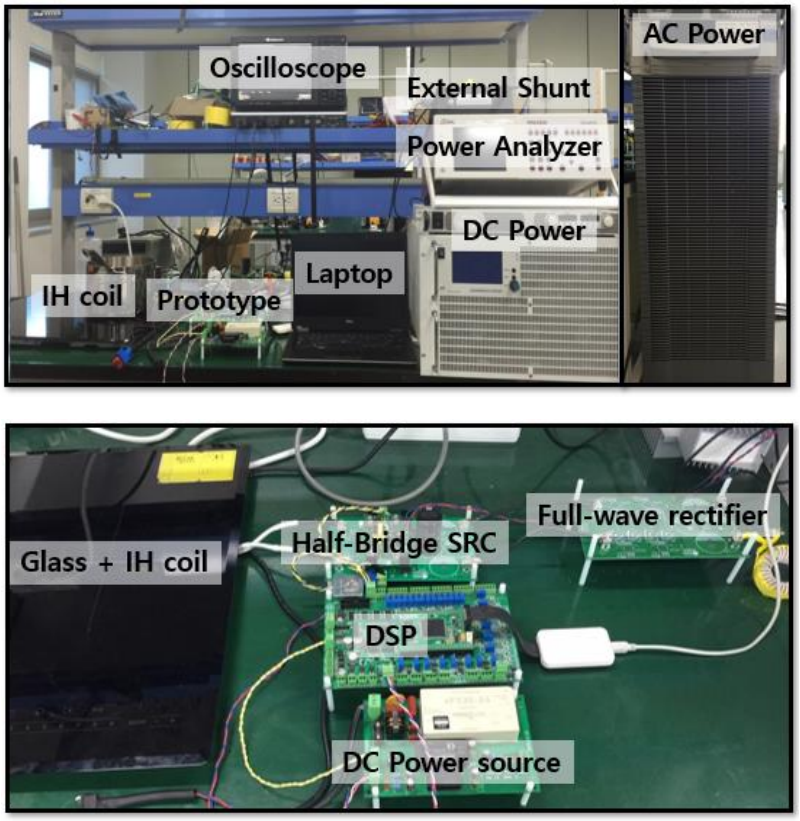

Fig. 19. Experimental setup of 3 kW prototype conventional IH system

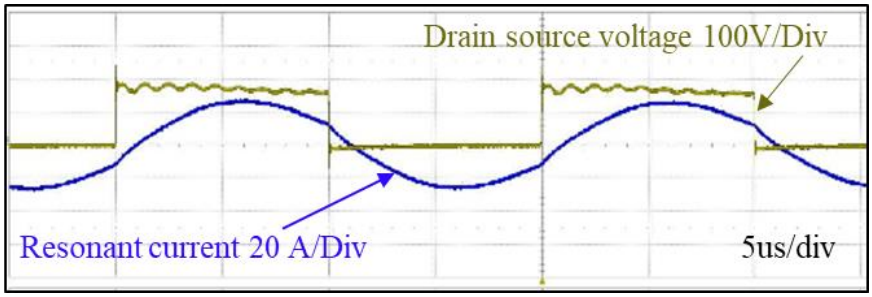

(a)

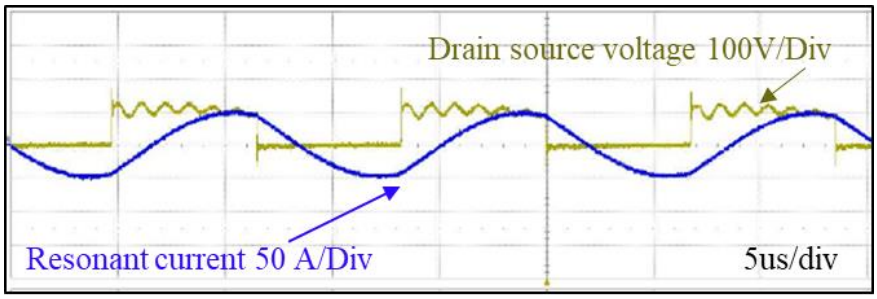

(b)

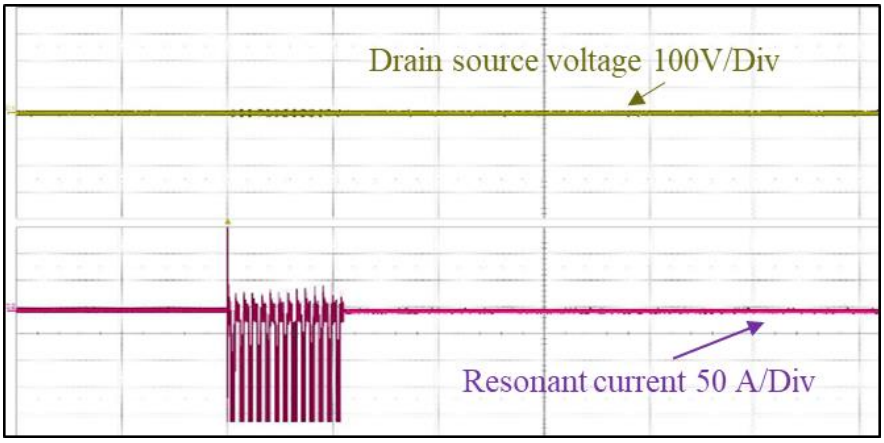

(c)

Fig. 20. Experimental results of conventional SRC for induction cooktop: (a) SUS-304 18-8, (b) SUS-304 18-10, (c) Aluminum

are analyzed by PSIM simulation based on the 3 kW rated power that achieves the heating speed of the universal induction cooktop. STS-304 18-8, STS-304 18-10, and aluminum material induce switch current 40 A, 59 A, and 100 A, respectively. In the case of STS-304 18-10 and aluminum material, the switch device and package price raises up due to very high switch heat, or it is impossible to implement as real converter. The experiment design specifications of conventional IH system is shown in TABLE III. Fig. 19 shows experimental setup of 3 kW conventional IH prototype which includes an the IH working coil under an the IH load, a digital controller (TMS320F28335), a AC power supply (KIKUSUI PCR6000LA), and a power converter. In addition, oscilloscope (Teledynelecroy Waverunner610Zi), and power analyzer (N4L PPA5530) are used to measure experimental results. Fig. 20 shows the

TABLE IV EXPERIMENTAL RESULT OF CONVENTIONAL IH SYSTEM

SUS-304 18-8	Input Voltage, V_i	220 Vdc	Input Current, I_i (RMS)	13.50 A
	Transmission Power, P_o	2.97 kW	Switch current (RMS)	40.06 A
SUS-304 18-10	Input Voltage, V_i	220 Vdc	Input Current, I_i (RMS)	13.54 A
	Transmission Power, P_o	2.98 kW	Switch current (RMS)	59.07 A
Aluminum	Input Voltage, V_i	220 Vdc	Input Current, I_i (RMS)	Burn-out
	Transmission Power, P_o	Burn-out	Switch current (RMS)	Burn-out

TABLE V LOSS ACCORDING TO SWITCH PACKAGE TYPE

Parameters	TO-247	TO-264	SOT-227
Conduction Loss	49.48 [W]	51.90 [W]	28.97 [W]
Switching Loss	10.71 [W]	10.31 [W]	2.51 [W]
Total Switching Loss	66.72 [W]	66.95 [W]	36.82 [W]
Junction Temperature	119.74 [℃]	94.63 [℃]	31.44 [℃]

experimental results of the conventional SRC for induction cooktop according to material of the vessel. TABLE IV describes the experimental results of 3 kW conventional IH prototype. The experimental results are similar to the simulation results. The STS-304 18-8 and STS-304 18-10 materials have a switch current of 40 A and 60 A, respectively. However, in the case of the aluminum material, when using the typically used RMS 60 A MOSFET switch, the switch device is burn-out due to high switch current shown in Fig. 20 (c). In order to heat it steadily, there is a great increase in the cost of switching devices with rated currents of peak 200 A and RMS 150 A, as well as a cooling system that can dissipate the heat.

Ⅲ. SRC for all-metal induction cooktop

To heat the non-ferromagnetic material, various research have been proposed [22-25]. As representative examples are the high-frequency operation method [26] and the THM method. Both methods increase the effective resistance of the vessel by lowering the skin depth of the vessel. A method of amplifying the frequency applied to the IH working coil was used to lower the skin depth of the vessel. In this section, the two representative methods for all-metal induction heating technology are analyzed. The operational principles, design considerations and strengths and weaknesses are introduced.

3.1 HFO

The HFO method simply increases the switching frequency to decrease the skin depth of the vessel to increase the load equivalent load resistance. Fig. 21 shows the equivalent load resistance of the

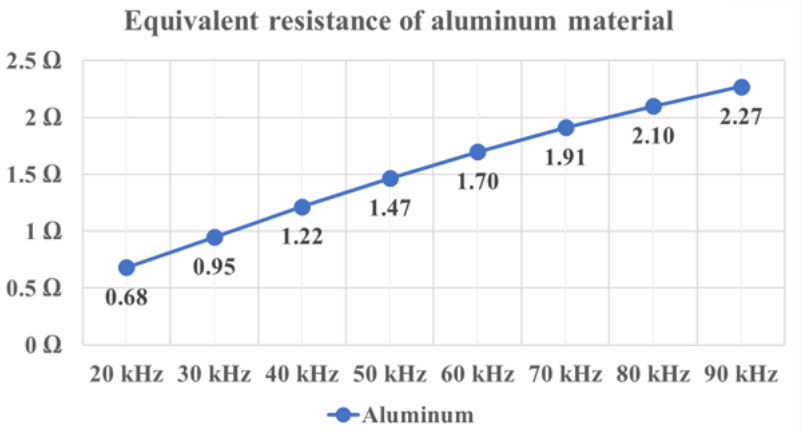

Fig. 21. Switching device according to package type for HFO

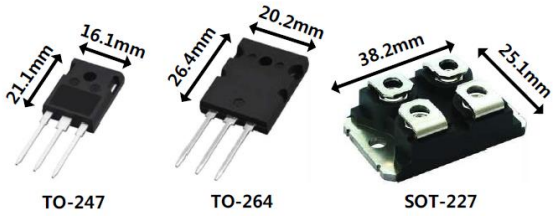

Fig. 22. Switching device according to package type for HFO

vessel according to the operating frequency of each material. However, the switching frequency operated in HFO method causes high switching losses, resulting in high temperature in the switch. This not only increases the switch rated current but also raises the cost for the switch cooling system which relieves a switch heat. Fig. 22 shows switching device according to package type for HFO method. In the HFO method, SiC device is used to reduce a heat in switch due to high frequency switching. SiC device has the lower switching losses at the same switching frequency due to their lower on-resistance compared to the other devices such as MOSFET. Therefore, the HFO method compensated for the drawbacks due to the high switching frequency by using a SiC device with low switching losses.

3.2 THM

In the previous research, the THM method is proposed in 2016. A common challenge of all-metal induction heating technology is to reduce the switch current by increasing the load equivalent load resistance. The method of increasing the load equivalent load resistance in IH inverter is to increase the number of turns in primary and the operating frequency of the current induced to the IH working coil. However, increasing the number of turns in primary has limitation by increasing the coil size and coil conduction loss which is dominant in the loss of the IH inverter. And Increasing the switching frequency to increase the operating frequency induced to the IH working coil increases the switching loss such as

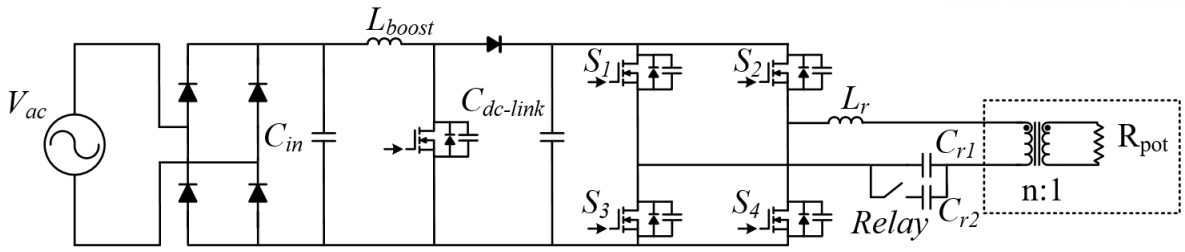

Fig. 23. Circuit diagram of THM method

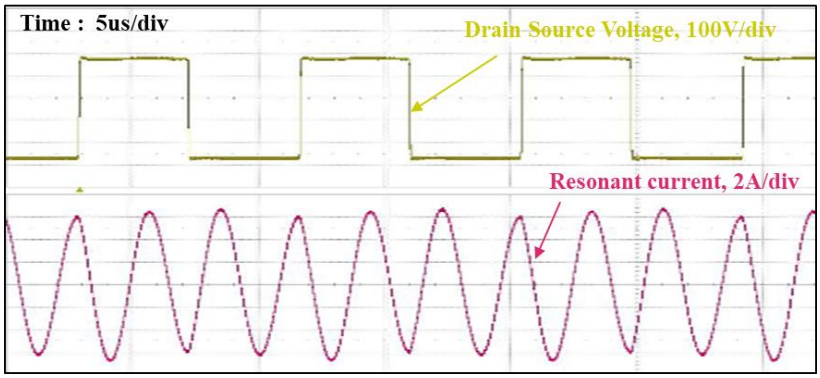

Fig. 24. Experimental results of THM method

a turn-on and turn-off loss. In THM method, in order to apply the high frequency current to the IH working coil without increasing the switch frequency, the series resonant network of the IH inverter is designed with the third harmonic filter. At the bridge circuit, the current with switching frequency is generated, and the third harmonic components is filtered by passing through the third harmonic series resonant network. Thus, the frequency of current induced to the IH coil is three times higher switching frequency is generated. Fig. 23 shows the circuit diagram of the THM method. The THM scheme includes the front-end active PFC, the full-bridge structure and resonant network with relay. The THM method change the resonant capacitor according to the material of the vessel by using relay. the resonant capacitor C_{r1} is used to heat the ferromagnetic material and the resonant capacitor is formed of C_{r1} and C_{r2} when the non-ferromagnetic material heated. In this research, the SRC with THM method is designed with a switching frequency of 25 kHz and a resonant frequency of the series resonant network of 75 kHz. The design procedures of THM resonant inverter is similar to a typical IH inverter. The switching frequency is described as follow:

$$f_s = \frac{1}{2\pi\sqrt{L_r C_r}} \tag{11}$$

where f_s is the switching frequency, L_r is the resonant inductance, C_r is the resonant capacitance. The resonant capacitor C_{r1} and C_{r2} can be calculated as follows:

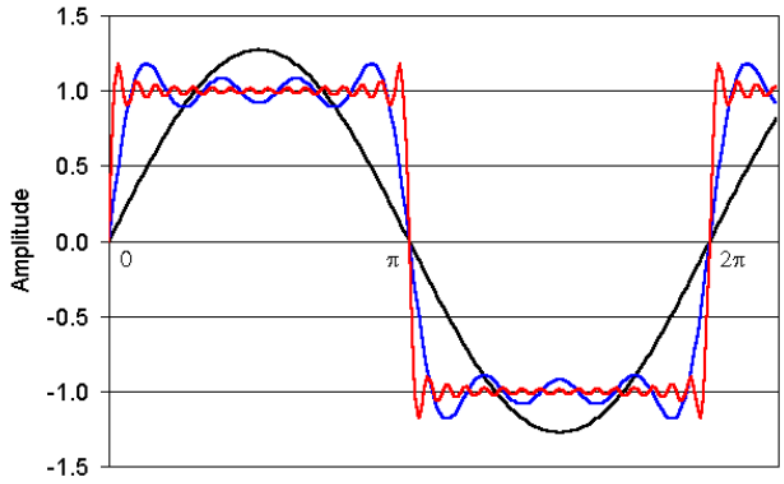

Fig. 25. Fourier series of square waveforms

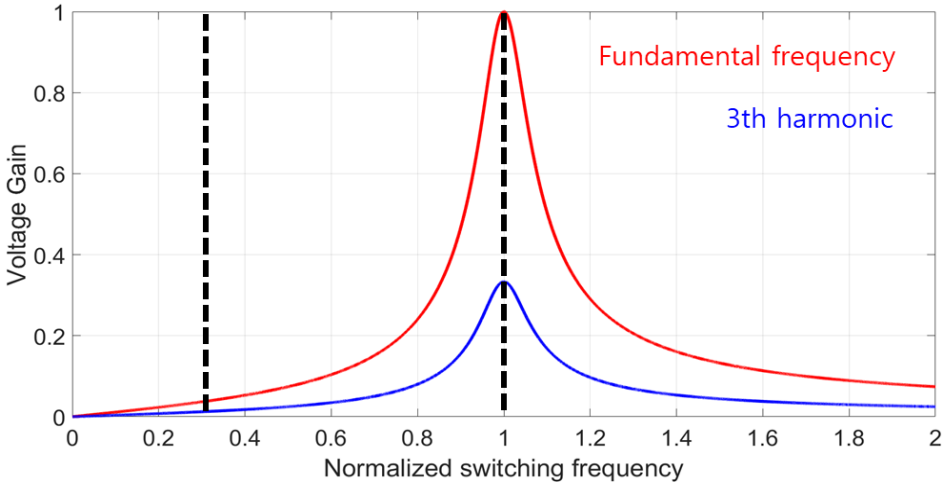

Fig. 26. First harmonic and third harmonic voltage gain curves

$$f_{sF} = \frac{1}{2\pi\sqrt{L_{rF}C_{r1}}} \tag{12}$$

$$f_{sNF} = \frac{1}{6\pi\sqrt{L_{rNF}(C_{r1}+C_{r2})}} \tag{13}$$

$$C_{r1}+C_{r2} = \frac{L_{rF}}{9\cdot L_{rNF}}\cdot C_{r1} \tag{14}$$

$$C_{r1} = \frac{1}{4\cdot\pi^2\cdot f_{sF}^2 L_{rF}} \tag{15}$$

$$C_{r2} = \frac{L_{rF}-9L_{rNF}}{9\cdot L_{rNF}}\cdot C_{r1} \tag{16}$$

where f_{sF} is the switching frequency when the ferromagnetic material is heated, L_{rF} is the resonant inductance of the ferromagnetic material, f_{sNF} is the switching frequency when the non-ferromagnetic

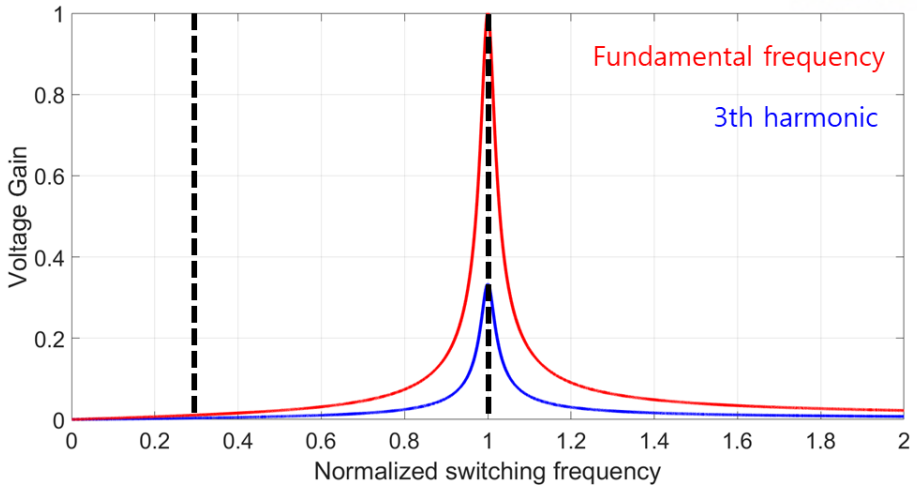

Fig. 27. First harmonic and third harmonic voltage gain curves at high Q-factor

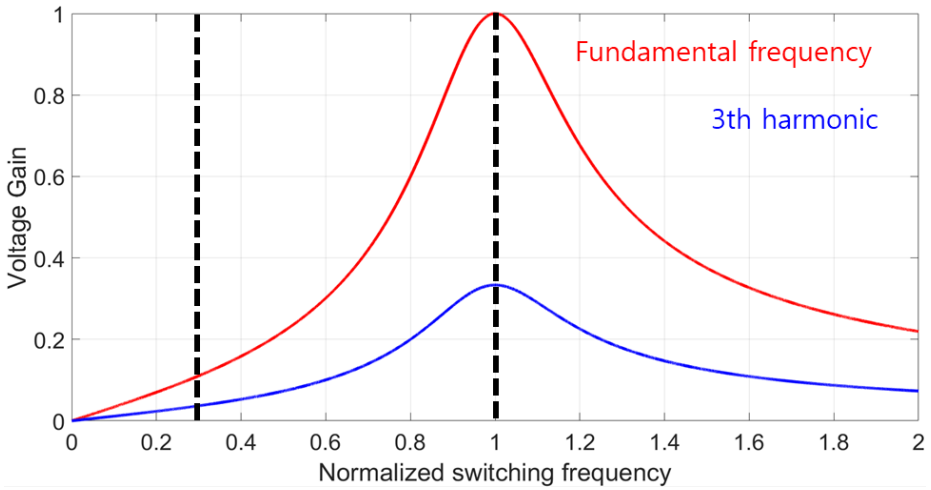

Fig. 28. First harmonic and third harmonic voltage gain curves at low Q-factor

material is heated, L_{rNF} is the resonant inductance of the non-ferromagnetic material. Fig. 24 shows experimental results of THM. It increases the equivalent load resistance by reducing skin-depth of the vessel. Therefore, the increased equivalent load resistance reduces the switching current of the IH inverter which reduces the switch rated current. Since the switching frequency of the THM method is maintained at the same level as that of the conventional IH inverter, the switching losses does not deteriorate as compared with the conventional one, as well.

However, the THM method has critical demerits. Fig. 25 shows the Fourier series of square waveforms. The Fourier series expansion of a square wave is indeed the sum of sines with odd-integer multiplies of the fundamental frequency. The third harmonic resonant network, which mainly filter the third harmonic components, remove the other harmonic components. The resonant network voltage gain of the THM method is reduced by about 1/3 shown in Fig. 26. Therefore, active power factor correction (PFC) is needed to compensate the reduced voltage gain of the resonant network in the THM method. In [27], the series resonant inverter which is combined with a power factor correction (PFC)

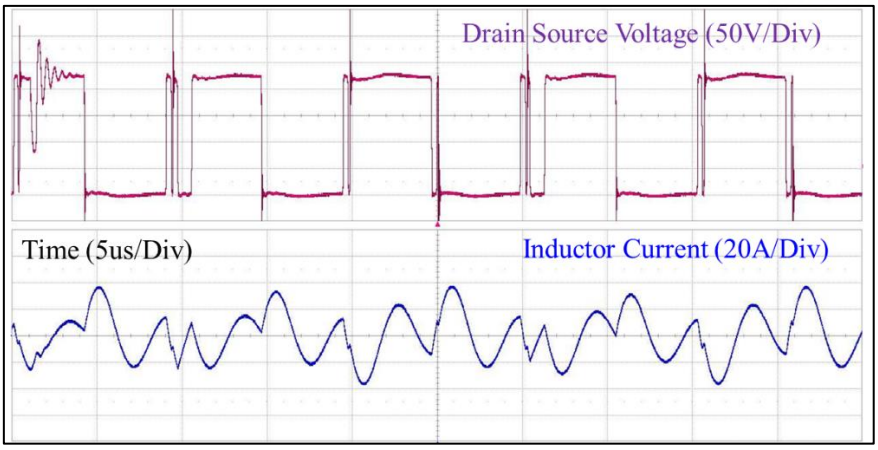

Fig. 29. Non-ZVS waveform of THM inverter affected by 1st harmonic

circuit is proposed. The PFC boost-up the input voltage from 350 Vdc to 450 Vdc, which compensates the small voltage gain of the resonant network according to the THM. However, it causes poor cost-effectiveness of the all-metal IH cooktop due to large passive components for the PFC. In addition, the Q-factor of the series resonant inverter for IH should be considered to implement the third harmonic method. Fig. 27 and Fig. 28 show the first harmonic and third harmonic voltage gain curves at high Q-factor and low Q-factor, respectively. In a series resonant inverter, the Q-factor determines the selectivity of the voltage gain. As shown in Fig. 27 and Fig. 28, the higher Q-factor, the less the effect of fundamental harmonics. The lower Q-factor, the smoother the slope of the voltage gain curve and the lower the selectivity of the voltage gain. Fig. 29 shows the non-ZVS waveform of the converter with THM method affected by the fundamental harmonic. As shown in Fig. 29, the third harmonic waveforms affected by the fundamental harmonic is distorted and the desired current waveform can not be obtained. Therefore, the ZVS operation is impossible. It leads to high heat to the switch, which makes unstable induction heating operation. The Q-factor formula that determines the stability of the third harmonic induction heating inverter is as follows:

$$Q = \frac{1}{R_{eq}} \sqrt{\frac{L_r}{C_r}} \tag{17}$$

where R_{eq} is the equivalent load resistance, L_r is the resonant inductance, C_r is the resonant capacitance. The high resonant inductance and low load equivalent load resistance are required to design the high Q-factor. Therefore, the THM method has design constraints that require to design the IH working coil with high leakage inductance.

3.3 Simulation & experimental results

In this section, the theoretical analysis is validated by using PSIM simulation and 2 kW prototype IH

TABLE VI SIMULATION DESIGN SPECIFICATIONS OF HFO IH SYSTEM

Transmission Power, P_o		2.0 kW	SUS-304 18-8 Resistance of vessel	1.8 Ω, at 27.7 kHz
Input Voltage, V_i		220 Vdc	Aluminum Resistance of vessel	1.5 Ω, at 110 kHz
Turn numbers, N		19 turns		
SUS-304 18-8	Resonant Inductance, L_r	27.2 uH	Resonant Frequency, f_r	25.8 kHz
	Resonant Capacitance, C_r	1,399 nF	Switching Frequency, f_s	27.7 kHz
Aluminum	Resonant Inductance, L_r	16.9 uH	Resonant Frequency, f_r	100 kHz
	Resonant Capacitance, C_r	150 nF	Switching Frequency, f_s	110 kHz

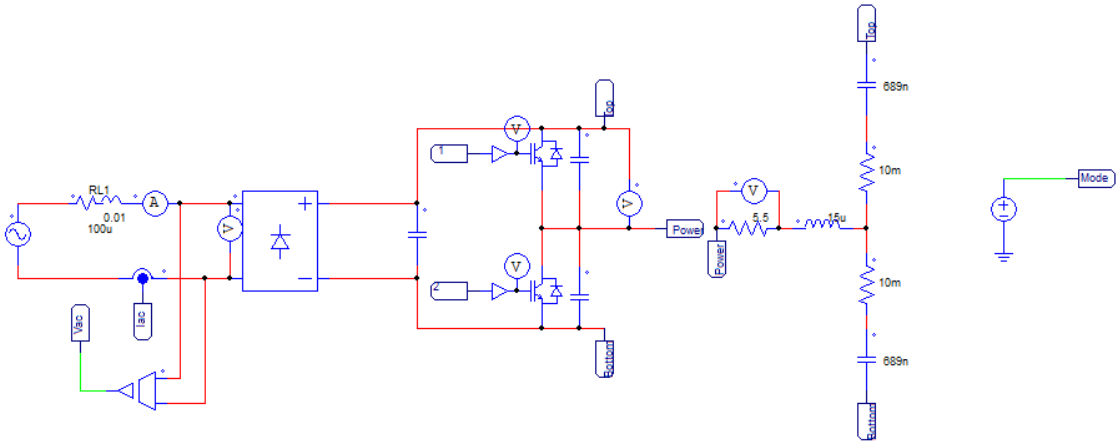

Fig. 30. Simulation model of HFO method

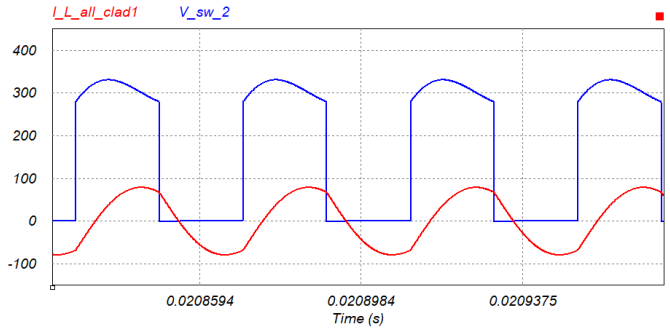

(a)

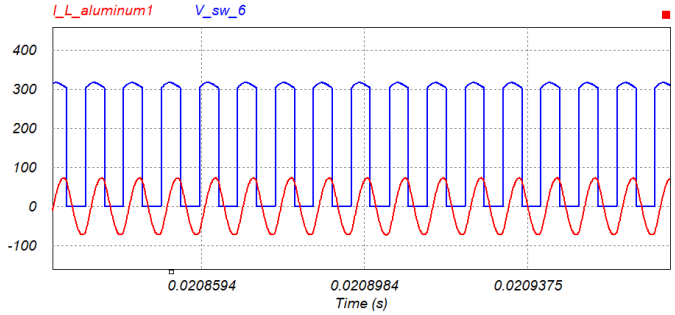

(b)

Fig. 31. Simulation waveforms of HFO method: (a) STS-304 18-8, (b) Aluminum

TABLE VII SIMULATION RESULTS OF HFO IH SYSTEM

SUS-304 18-8	Input Voltage, V_i	220 Vdc	Input Current, I_i (RMS)	9.2 A
	Transmission Power, P_o	2.0 kW	Switch current (RMS)	28.06 A
Aluminum	Input Voltage, V_i	220 Vdc	Input Current, I_i (RMS)	9.1 A
	Transmission Power, P_o	2.0 kW	Switch current (RMS)	38.64 A

TABLE VIII SIMULATION DESIGN SPECIFICATIONS OF THM IH SYSTEM

Transmission Power, P_o			2.0 kW	SUS-304 18-8 Resistance of vessel	2.3 Ω, at 27.7 kHz
Input Voltage, V_i			350 ~ 450 Vdc	Aluminum Resistance of vessel	1.8 Ω, at 85 kHz
Turn numbers, N			41 turns		
SUS-304 18-8		Resonant Inductance, L_r	22 uH	Resonant Frequency, f_r	25.8 kHz
		Resonant Cap., C_r	1,579 nF	Switching Freq., f_s	33.5 kHz
Aluminum	Low Q	Resonant Inductance, L_r	16 uH	Resonant Frequency, f_r	83 kHz
		Resonant Cap., C_r	229 nF	Switching Freq., f_s	28.3 kHz
	High Q	Resonant Inductance, L_r	130 uH	Resonant Frequency, f_r	83 kHz
		Resonant Cap., C_r	28.2 nF	Switching Freq., f_s	28.3 kHz

inverter. The overall simulation model of the HFO method is shown in Fig. 30, which consists of a diode rectifier, the half-bridge structure, the resonant network with relay which change the resonant capacitor according to the material of the vessel. This simulation TABLE VI describes the simulation design specifications of the HFO method. This simulation is based on the HFO using MOSFET devices.

The design specifications are based on the resonant inductance and the load equivalent load resistance measured by using the RLC meter. The switching frequency is set to 100 kHz. The equivalent load resistance of the aluminum vessel measured at 100 kHz is 2.1 Ω, which is capable of heating 2 kW with a half-bridge input voltage. The SUS-304 18-8 vessel, which is a representative example of the ferromagnetic material, is the same as the conventional IH inverter design specifications. Fig. 31 shows the simulation waveforms of the HFO method. As shown in Fig. 31, both SUS-304 18-8 and aluminum materials achieved the ZVS operation. TABLE VII describes the simulation results of HFO IH system. Both non-ferromagnetic material vessel and ferromagnetic material vessel achieved the desired power 2 kW while satisfying the switch rated current of 40 A. The simulation results show that all-metal IH technology capable of heating the aluminum material. However, if the switch heat is high, the cost of the switch device and package increase to operate stably. Switching loss, which is the main cause of switching heat, will be compared with the THM method after the THM method simulation analysis.

TABLE VIII shows the simulation design specifications of THM IH system. For a fair comparison with the HFO method, the resonant frequency of the non-ferromagnetic material is set to be the same. Fig. 32 shows the simulation model of the THM method. The THM method consists of active PFC, full-bridge structure and resonant network. The active PFC compensates for the insufficient voltage

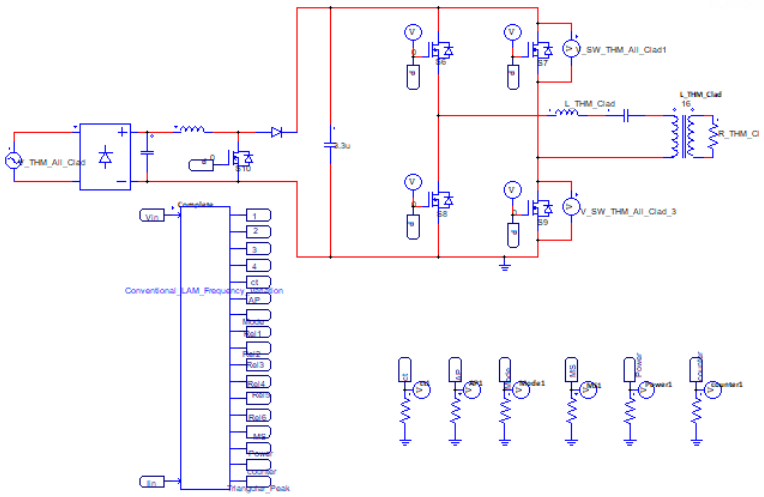

Fig. 32. Simulation model of THM method

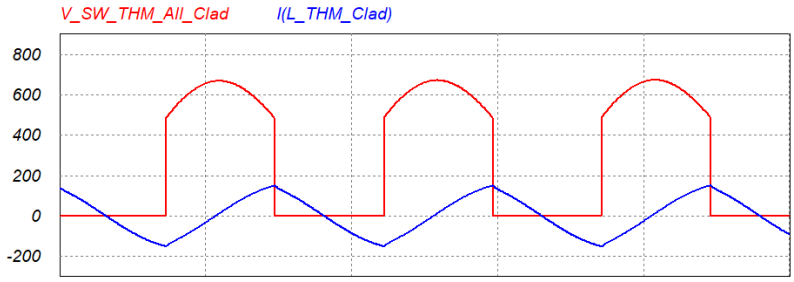

(a)

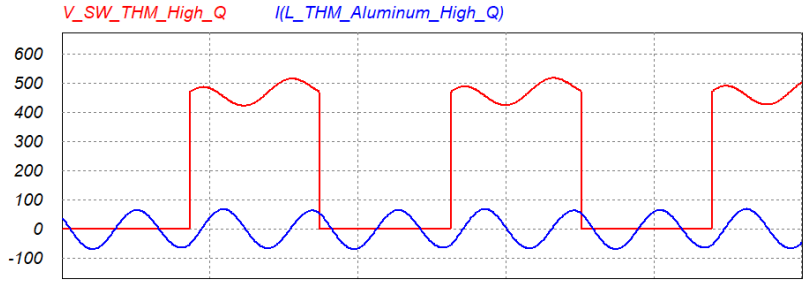

(b)

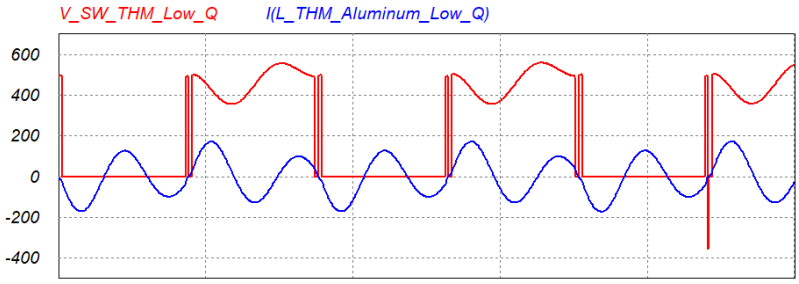

(c)

Fig. 33. Simulation waveforms of THM method

(a) STS-304 18-8, (b) Aluminum (high Q-factor), (c) Aluminum (low Q-factor)

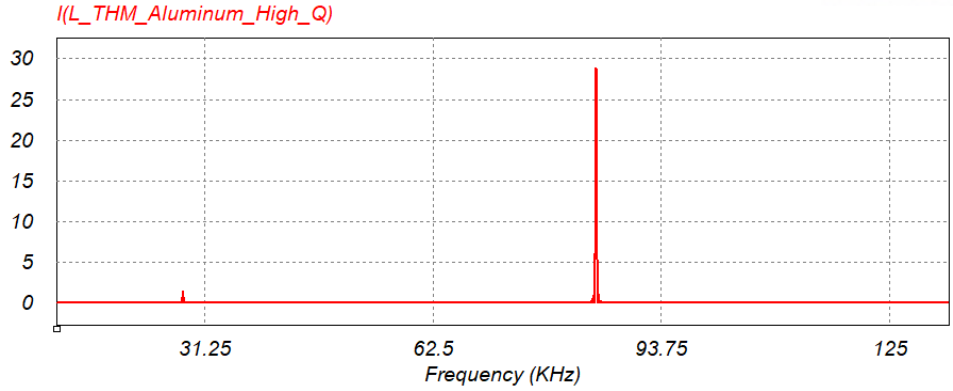

(a)

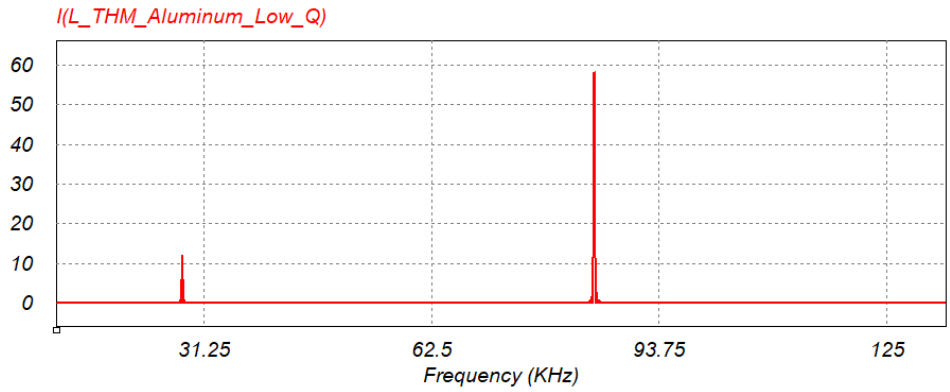

(b)

Fig. 34. FFT simulation of THM method with high Q-factor and low Q-factor
(a) High Q-factor, (b) Low Q-factor

gain of the resonant network during the THM operation to heat the non-ferromagnetic material. The switching frequency for heating the non-ferromagnetic material is designed as the three times smaller than its resonant frequency. And input voltage is boosted up to 450 Vdc which compensates the voltage drop due to the third harmonic operation. Fig. 33 shows the simulation waveforms of the THM method.

The conventional IH inverter which use the first harmonic resonant network is used for heating the ferromagnetic material SUS-304 18-8. When the non-ferromagnetic material is heated, the period of the switch current appears three times in one switching cycle, and the ZVS operation is achieved. It is achieved by designing with the high Q-factor which makes the first harmonic effect small. Fig. 33, (c) shows the simulation waveforms of the THM method with low Q-factor, designed with the IH working coil which has the low coil inductance. By designing with the low Q-factor, the effect of the first harmonic becomes large, distorting the switching current waveform. It causes that the ZVS operation was not achieved. Fig. 34 shows the FFT simulation of THM method with high Q-factor and low Q-factor. As shown in Fig. 34, in the low Q-factor condition, the first harmonic effect around 30 kHz band is bigger than the high Q-factor condition. As analyzed in the previous section, the stability of operation

TABLE IX SIMULATION RESULTS OF THM IH SYSTEM

SUS-304 18-8		Input Voltage, V_i	450 Vdc	Input Current, I_i (RMS)	9.2 A
		Transmission Power, P_o	2.0 kW	Switch current (RMS)	28.06 A
Aluminum	High Q-factor	Input Voltage, V_i	350 Vdc	Input Current, I_i (RMS)	9.1 A
		Transmission Power, P_o	2.0 kW	Switch current (RMS)	38.64 A
		1st harmonic magnitude	1.43		
	Low Q-factor	Input Voltage, V_i	350 Vdc	Input Current, I_i (RMS)	9.1 A
		Transmission Power, P_o	2.0 kW	Switch current (RMS)	38.64 A
		1st harmonic magnitude	12.00		

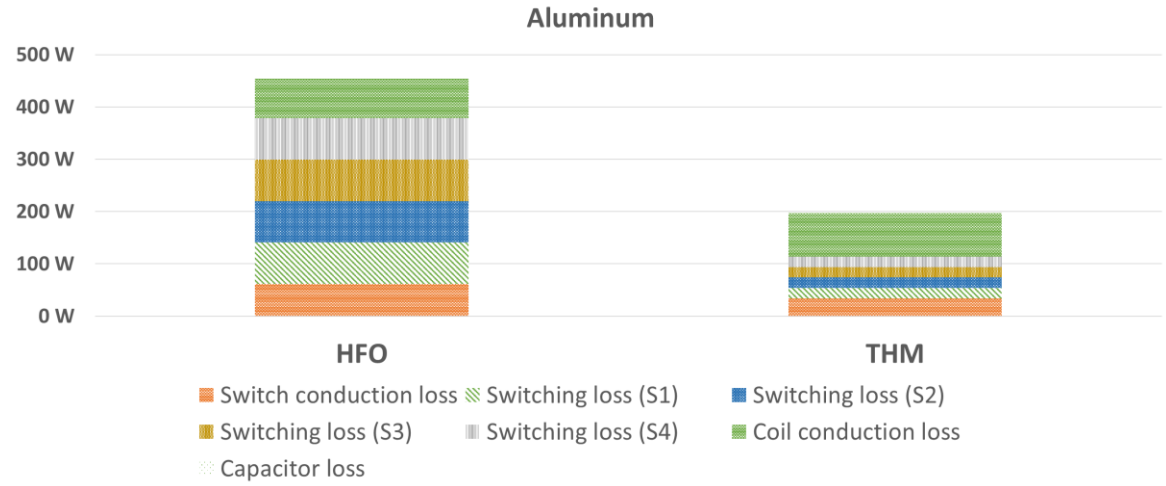

(a)

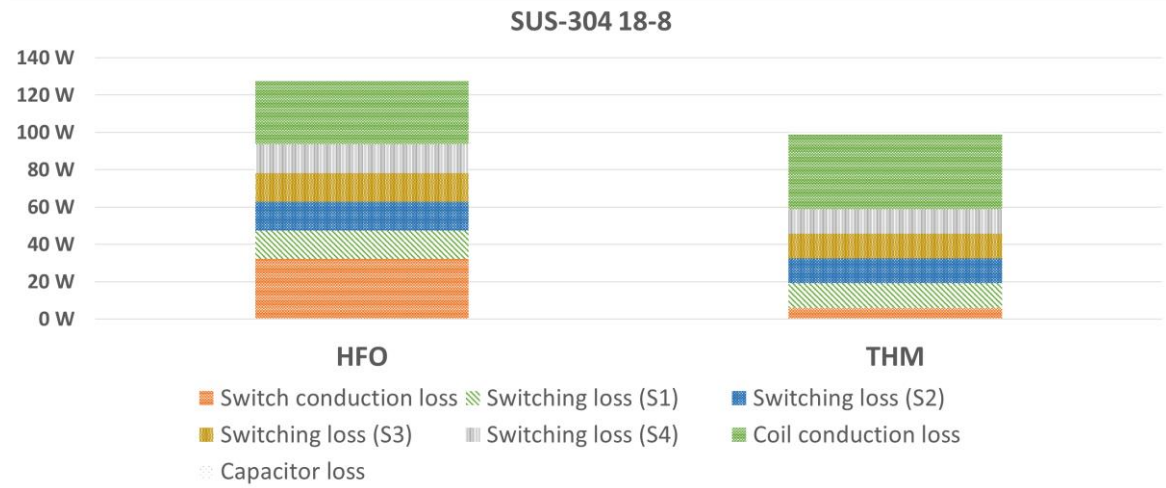

(b)

Fig. 35. Comparison loss data of HFO and THM method: (a) Aluminum, (b) SUS-304 18-8

in the THM method is determined by the Q-factor of the SRC. TABLE IX describes the simulation results of the THM method. As described in TABLE IX, the THM method achieves the desired power 2 kW while satisfying the switch rated current 40 A by controlling the input voltage and the frequency

TABLE X EXPERIMENT DESIGN SPECIFICATION OF THM IH SYSTEM

Transmission Power, P_o			2.0 kW	SUS-304 18-8 Resistance of vessel	2.2 Ω, at 27 kHz
Input Voltage, V_i			350 ~ 450 Vdc	Aluminum Resistance of vessel	1.8 Ω, at 84 kHz
Turn numbers, N			41 turns		
SUS-304 18-8		Resonant Inductance, L_r	22 uH	Resonant Frequency, f_r	26.8 kHz
		Resonant Cap., C_r	1,600 nF	Switching Freq., f_s	30.5 kHz
Aluminum	Low Q	Resonant Inductance, L_r	16 uH	Resonant Frequency, f_r	82.9 kHz
		Resonant Cap., C_r	230 nF	Switching Freq., f_s	28 kHz
	High Q	Resonant Inductance, L_r	130 uH	Resonant Frequency, f_r	80.5 kHz
		Resonant Cap., C_r	30 nF	Switching Freq., f_s	28 kHz

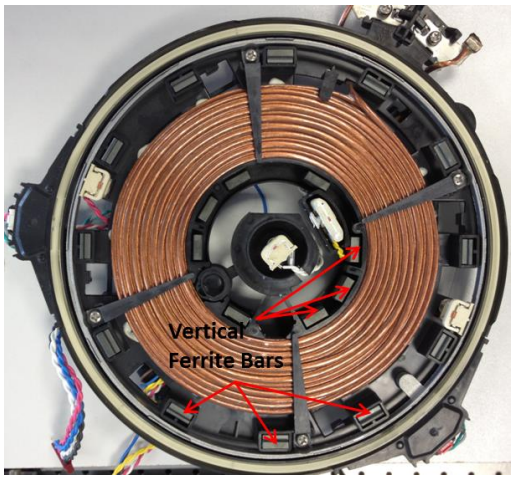

Fig. 36. All-metal IH working coil manufactured by Hitachi, Ltd

induced the IH working coil according to the material of the vessel. The simulation results how that all-metal IH technology capable of heating the aluminum material. Fig. 35 shows the comparison loss data of HFO and THM method. It includes the switching loss which is turn-on and turn-off loss, switch conduction loss, switch capacitor loss, and the IH working coil conduction loss. For the technical performance comparison, the loss analysis was implemented based on the same MOSFET device. In shown as Fig. 35, the THM method has the lower switch loss, which includes the turn-on and turn-off loss and switch conduction loss, than the HFO method in the same desired power condition. As in the simulation, if the HFO method is implemented by using the MOSFET device, stable operation cannot be guaranteed due to the high switch heat. It is not possible to implement the HFO method using MOSFET in IH technology which should operate stably for a long time. The SiC-based HFO optimization is a technology to compensate for high switch heat due to high switching frequency, which is distant from the technological advanced of all-metal IH technology. The HFO method is the solution for improving performance that can be combined with other all-metal technologies such as the THM method. Therefore, the industry adopts the THM method as the most advanced technology. The LAM

TABLE XI EXPERIMENT RESULTS OF THM IH SYSTEM

SUS-304 18-8		Input Voltage, V_i	450 Vdc	Input Current, I_i (RMS)	4.44 A
		Transmission Power, P_o	2.0 kW	Switch current (RMS)	26.55 A
Aluminum	High Q-factor	Input Voltage, V_i	350 Vdc	Input Current, I_i (RMS)	5.70 A
		Transmission Power, P_o	2.0 kW	Switch current (RMS)	40.50 A
	Low Q-factor	Input Voltage, V_i	350 Vdc	Input Current, I_i (RMS)	Burn-out
		Transmission Power, P_o	Burn-out	Switch current (RMS)	Burn-out

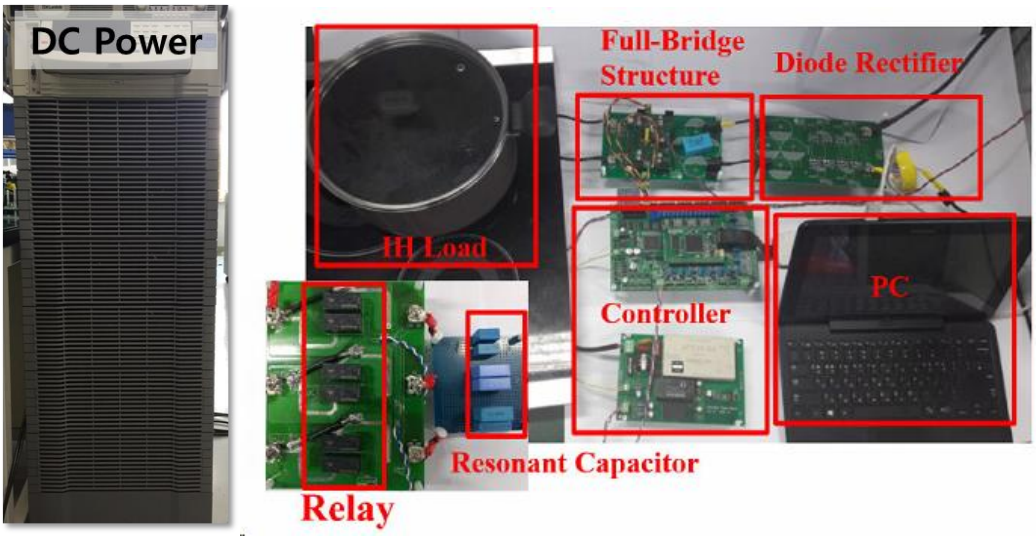

Fig. 37. Experimental setup of 2 kW prototype THM IH system

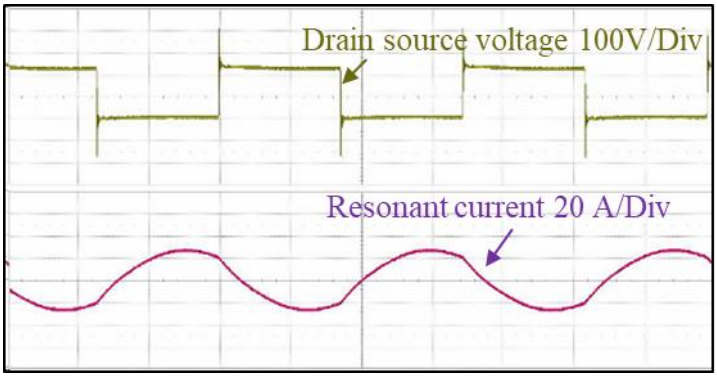

Fig. 38. Experimental results of THM method (SUS-304 18-8)

proposed in the next section will be compared with the THM method.

TABLE X describes the experiment design specification of THM IH system. Since the simulation design specification TABLE VIII is based on the experimental setup TABLE X, they two design specifications are similar. Fig. 36 shows the all-metal IH working coil manufactured by Hitachi, Ltd., used for the THM method [28-29]. The all-metal IH working coil is fabricated the high coil turns in primary. In the THM method, since the high Q-factor is required, the high coil inductance is needed. In addition, due to the active PFC, the DC-link voltage uses 350 to 450 Vdc, which is higher the 220 Vdc

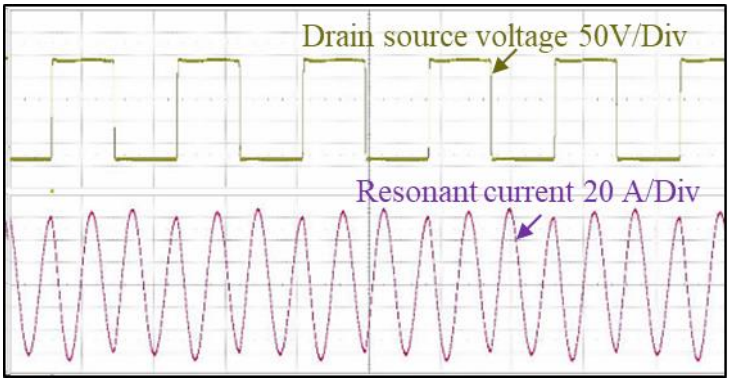

(a)

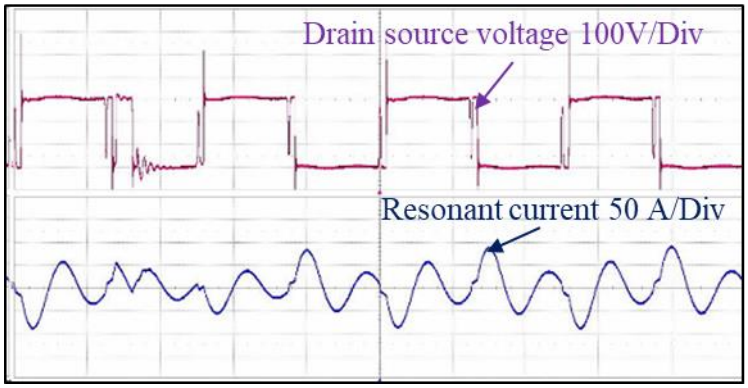

(b)

Fig. 39. Experimental results of THM method according to Q-factor
(a) Aluminum (high Q-factor), (b) Aluminum (low Q-factor)

used in the conventional IH system. Therefore, a high load equivalent load resistance should be produced with a high number of IH working coil turns to satisfy the desired power. Fig. 37 shows the experimental setup of the 2 kW prototype for THM IH system. In shown Fig. 37, the DC power supply was used to replace the active PFC. Fig. 38 shows experimental results of the THM method when heating the ferromagnetic material SUS-304 18-8. Fig. 39 shows experimental results of the THM method according to Q-factor. As the simulation results, both SUS-304 18-8 and aluminum material is heated while satisfying the desired power and switch rated current 40 A. However, the ZVS operation was not achieved in the low Q-factor condition. Experiment designed with a low Q-factor were burned out due to the high switch heat after a short period of heating. As a result, the all-metal IH performance and functional limits of the THM method were verified by implementing the experiment.

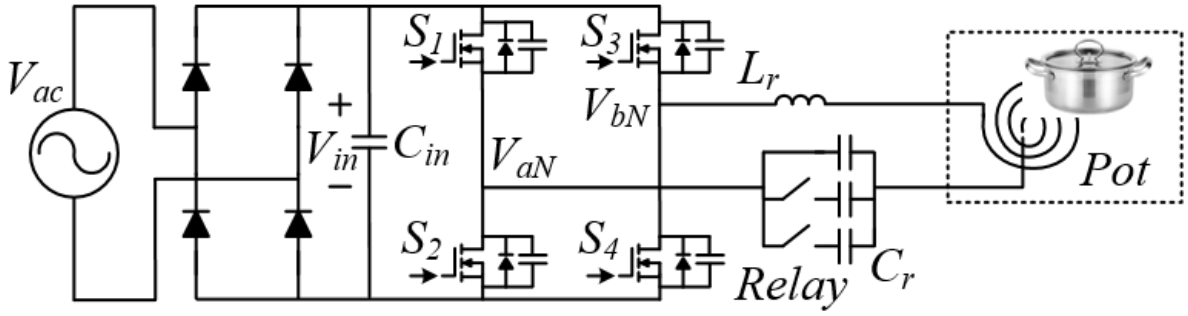

Fig. 40. Circuit diagram of LAM

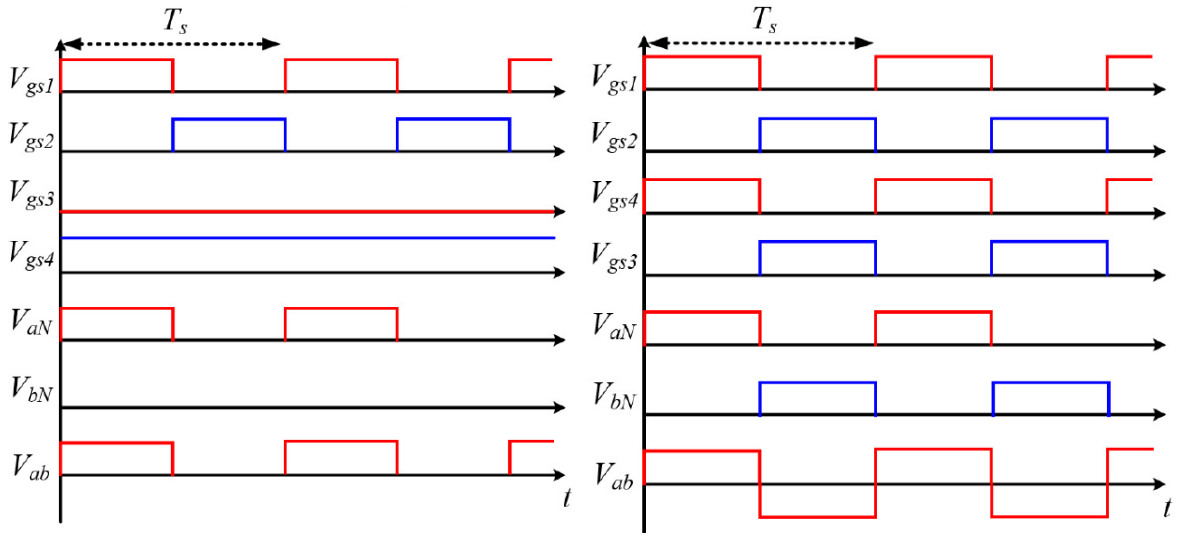

(a) (b)

Fig. 41. Conceptual waveforms of input voltage controlling mode in LAM:
(a) Half-bridge mode, (b) Full-bridge mode

IV. Analysis and design of LAM

In this section, LAM is analyzed which can solve a cost issue of the all-metal IH technology, and obtain the heating capability for the ferro- and non-ferromagnetic materials. Fig. 40 shows the circuit diagram of the LAM which includes the full-bridge structure and the resonant network with relays. This resonant network can control the resonant frequency according to material of vessels. The LAM has four modulation modes which change the input voltage and the operating frequency induced to the IH working coil. These modulation modes are changed according to the material of the vessel. where Vac is the AC input voltage, V_{aN} and V_{bN} are the leading leg between S1 and S2, and the lagging lag between S3 and S4, respectively. In the LAM, the all-metal IH working coil manufactured by Hitachi, which is used to implement the THM method, was selected for a fair comparison evaluation. In this section, the design methodology, operational principles and performance evaluation of the LAM is analyzed.

4.1 Proposed modulation modes

Fig. 41. shows the conceptual voltage waveforms of the input voltage controlling mode in the LAM. These modes are operating modes to compensate for the difference in heating performance due to the resistance difference of the ferromagnetic material. Among the vessel made of ferromagnetic material, there is a resistance difference according to the manufacturer. In the LAM, it is possible to heat the ferromagnetic materials as the desired power by changing the modulation mode according to the material of the vessel. In the full-bridge mode, the bridge voltage V_{ab} is maintained as level of the input voltage. At the resonant frequency, the vessel can be approximated as a resistance, and the voltage gain of the resonant network is unity. The transmission power of the full-bridge mode is described as follows:

$$P_{fb,\max} = \frac{V_{in}^2}{R_{pot,f}} \tag{18}$$

where $P_{fb,max}$ is the transmission power of the full-bridge mode, V_{in} is the input voltage, and $R_{vessel,f}$ is the equivalent load resistance of vessel measured at the switching frequency. The minimum switching frequency which makes the maximum voltage gain of the resonant network is derived as the resonant frequency, which can be derived as follow:

$$f_{s,f,\min} = f_r = \frac{1}{2\pi\sqrt{L_r C_r}} \tag{19}$$

where f_r is the resonant frequency, $f_{s,f,min}$ is the minimum switching frequency of the full-bridge mode, C_r is the resonant capacitor, and L_r is the coil inductance. The conceptual waveform of the half-bridge mode is shown in Fig. 41 (a). In the half-bridge mode, the bridge voltage V_{aN} is a half of the input voltage. The transmission power of the half-bridge mode is four times smaller than the full-bridge mode as follow:

$$P_{hb,\max} = \frac{V_{in}^2}{4 \cdot R_{pot,h}} \tag{20}$$

where $P_{hb,max}$ is the transmission power of the half-bridge mode, $R_{vessel,h}$ is the equivalent load resistance of vessel of the half-bridge mode. The resonant frequency of the half-bridge mode is designed as the same resonant frequency of the full-bridge mode. Fig. 42. shows the conceptual waveforms of the frequency amplifying modes in the LAM. As shown in Fig. 42 (a), The frequency-doubling mode can obtain the operating frequency induced to the IH which is two times higher the switching frequency. As shown in Fig. 42 (a), the frequency-doubling mode amplifies the operating frequency induced to the IH working coil. And the frequency-doubling mode uses one pole of the full-bridge structure as a zero vector [30-33], so that the voltage gain is reduced to 1/2. The transmission power of the frequency-doubling mode can be derived as follow:

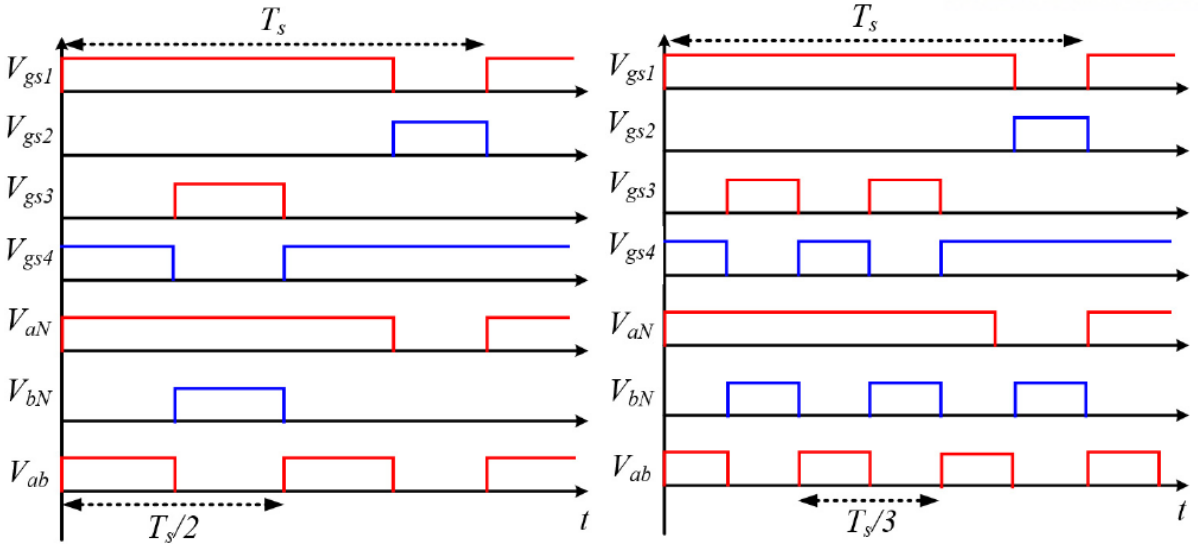

(a) (b)

Fig. 42. Conceptual waveforms of frequency amplifying mode in LAM:
(a) Frequency-doubling mode, (b) Frequency-triple mode

$$P_{d,\max} = \frac{V_{in}^2}{4 \cdot R_{pot,d}} \tag{21}$$

where $P_{d,max}$ is the transmission power of the frequency-doubling mode, and $R_{vessel,d}$ is the equivalent load resistance of vessel measured at the operating frequency which is two times higher switching frequency. The doubled operating frequency increases the effective resistance by reducing the skin-depth of the vessel. The frequency-doubling mode should design the resonant frequency twice the switching frequency. The resonant network of the frequency-doubling mode is combined with the elements of the fundamental harmonic filter used in the input voltage change modes. The resonant network design procedure of the frequency-doubling mode is similar to that of the THM method as follow:

$$f_{r,d} = f_{s,d,\min} = \frac{1}{4\pi\sqrt{L_{r,d}(C_r + C_{r,d})}} \tag{22}$$

$$(C_r + C_{r,d}) = \frac{L_r}{4 \cdot L_{r,d}} \cdot C_{r1} \tag{23}$$

$$C_{r,d} = \frac{L_r - 4 \cdot L_{r,d}}{4 \cdot L_{r,d}} \cdot C_r \tag{24}$$

where $f_{r,d}$ is the resonant frequency of the frequency-doubling mode, $f_{s,d,min}$ is the minimum switching frequency of the frequency-doubling mode, $L_{r,d}$ is the coil inductance at the doubled operating frequency, and $C_{r,d}$ is the resonant capacitor of the frequency-doubling mode. The design procedure of the frequency

triple mode is similar. As the frequency-doubling mode, since the voltage gain of the bridge voltage is reduced to 1/2, the transmission power of the frequency-triple mode is derived as follows:

$$P_{t,\max} = \frac{V_{in}^2}{4 \cdot R_{pot,t}} \tag{21}$$

where $P_{t,max}$ is the transmission power of the frequency-triple mode, $R_{vessel,t}$ is the equivalent load resistance of vessel measured at the tripled operating frequency. The resonant network design procedure of the frequency yripler mode is as follows:

$$f_{r,t} = f_{s,t,\min} = \frac{1}{6\pi\sqrt{L_{r,t}(C_r + C_{r,t})}} \tag{22}$$

$$(C_r + C_{r,t}) = \frac{L_r}{9 \cdot L_{r,t}} \cdot C_r \tag{23}$$

$$C_{r,t} = \frac{L_r - 4 \cdot L_{r,t}}{9 \cdot L_{r,t}} \cdot C_r \tag{24}$$

where $f_{r,t}$ and $f_{s,t,min}$ are the resonant frequency of the frequency-triple mode and the minimum switching frequency of the frequency-triple mode, respectively, $L_{r,t}$ is the coil inductance at the tripled operating frequency, and $C_{r,t}$ is the resonant capacitor of the frequency-triple mode.

4.2 Proposed algorithm

The LAM has the four modulation modes which have the different operating conditions for each mode by changing the bridge voltage or the frequency induced to the IH working coil. Each mode is selected according to the resistance of the vessel loaded on the IH working coil. In this section, the mode selection algorithm is analyzed. Fig. 43 shows the block diagram of the operational mode selection sequence. The maximum resistance of vessel of the full-bridge mode can be derived as follows:

$$R_{pot,f,\max} = \frac{G_{\max} \cdot V_{in}^2}{P_{rated}} \tag{25}$$

where G_{max} is the maximum voltage gain and P_{rated} is the desired power. The maximum resistance of vessel of the full-bridge mode is four times higher that of other modulation mode. The maximum resistance of vessel of the half-bridge mode is same to that of the frequency-doubling and triple modes as follows:

$$R_{pot,h,\max} = P_{pot,d,\max} = P_{pot,t,\max} = \frac{G_{\max} \cdot V_{in}^2}{4 \cdot P_{rated}} \tag{26}$$

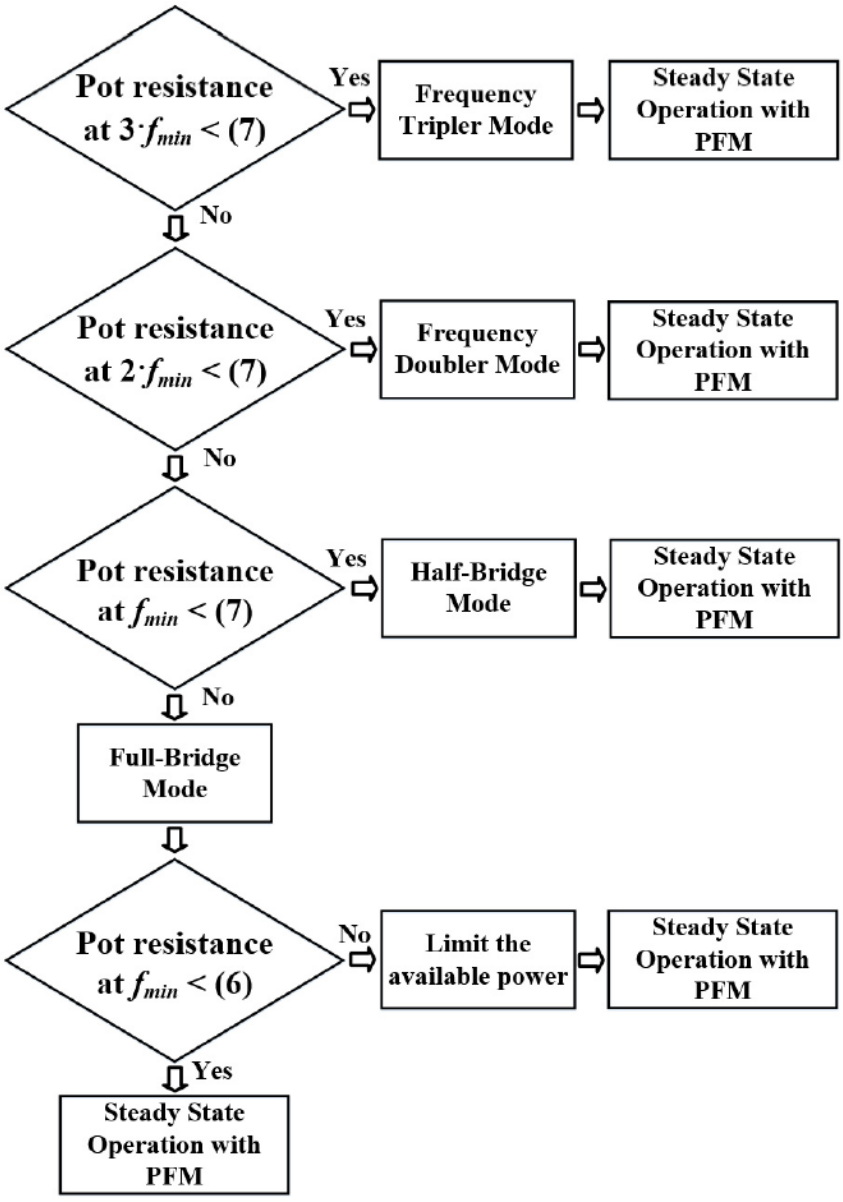

Fig. 43. Block diagram of operational mode selection sequence

The frequency-doubling and triple modes should satisfy (26) at the frequency which is two or three times higher switching frequency. When the equivalent load resistance of vessel is higher (26), the LAM inverter operates under the full-bridge mode. When the equivalent load resistance of vessel is satisfied with (26) at the frequency which is two or three times higher the switching frequency, the LAM inverter operates under the frequency amplifying modes. When the equivalent load resistance of vessel is satisfied with (26) at the switching frequency, the LAM inverter operates in the half-bridge mode. After the modulation mode is selected, the LAM inverter controls the transmission power using the pulse frequency modulation (PFM) [34-36]. If the digital controller senses no load and over current of the switch at the steady state, the LAM inverter resumes the proposed algorithm.

TABLE XII SIMULATION DESIGN SPECIFICATIONS OF LAM

Transmission Power, P_o		2.0 kW	Resistance of vessel, R_{vessel}	9.65 Ω, at 25 kHz
Input Voltage, V_i		220 Vdc	Resistance of vessel, R_{vessel}	3.16 Ω, at 25 kHz
Turn numbers, N		41 turns	Resistance of vessel, R_{vessel}	2.0 Ω, at 50 kHz
			Resistance of vessel, R_{vessel}	2.2 Ω, at 75 kHz
SUS-304 18-8	Resonant Inductance, L_r	160 uH	Resonant Frequency, f_r	25 kHz
	Resonant Capacitance, C_r	253 nF	Switching Frequency, f_s	28 kHz
SUS-304 18-10	Resonant Inductance, L_r	144 uH	Resonant Frequency, f_r	25 kHz
	Resonant Capacitance, C_r	253 nF	Switching Frequency, f_s	26 kHz
Aluminum	Resonant Inductance, L_r	129 uH	Resonant Frequency, f_r	50 kHz
	Resonant Capacitance, C_r	63.1 nF	Switching Frequency, f_s	52 kHz
Aluminum	Resonant Inductance, L_r	129 uH	Resonant Frequency, f_r	75 kHz
	Resonant Capacitance, C_r	28.1 nF	Switching Frequency, f_s	76.5 kHz

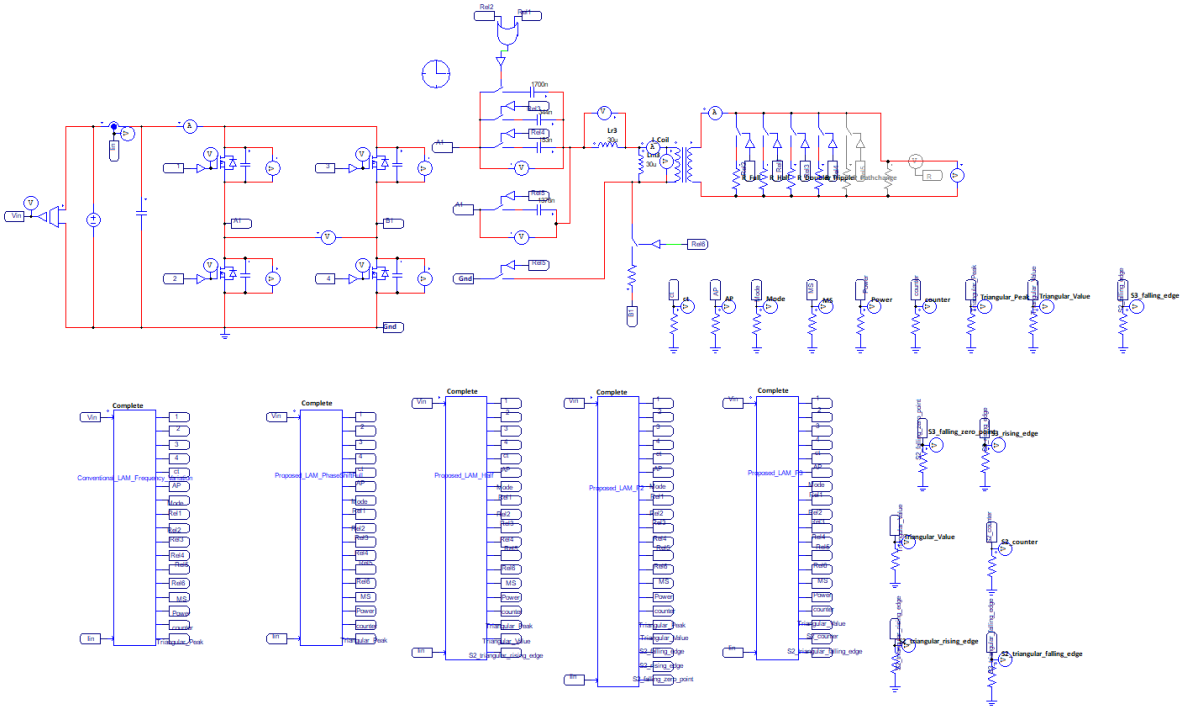

Fig. 44. Simulation model of the LAM

4.3 Simulation & experimental results

The design methodology and performance evaluation of a LAM is analyzed by using PSIM simulation and the 2 kW experimental prototype. The design specification of the proposed LAM is illustrated in TABLE XII. The minimum switching frequency is determined to 25 kHz. And the three vessel examples (SUS-304 18-8, SUS-304 18-10, Aluminum) are selected to test the proposed method. The PSIM simulation is used, which uses the same operational condition as the experimental

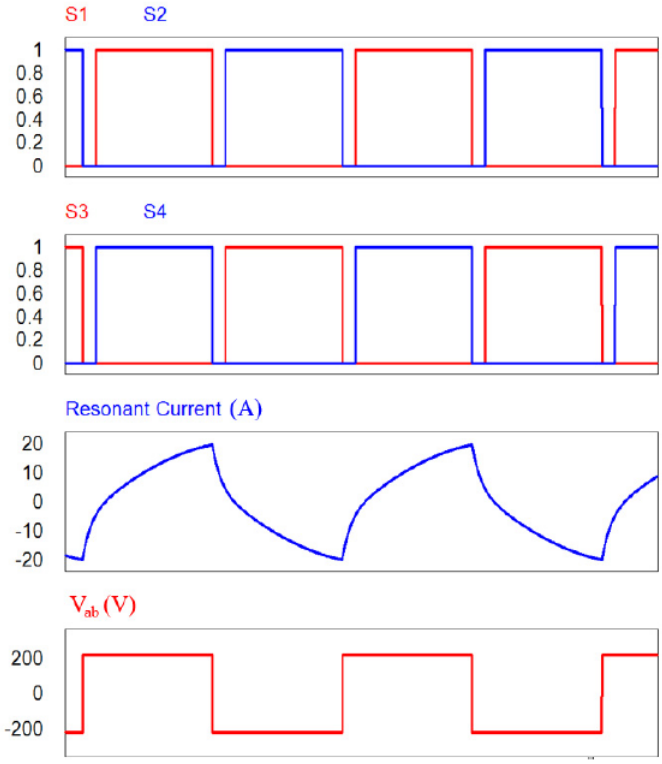

(a)

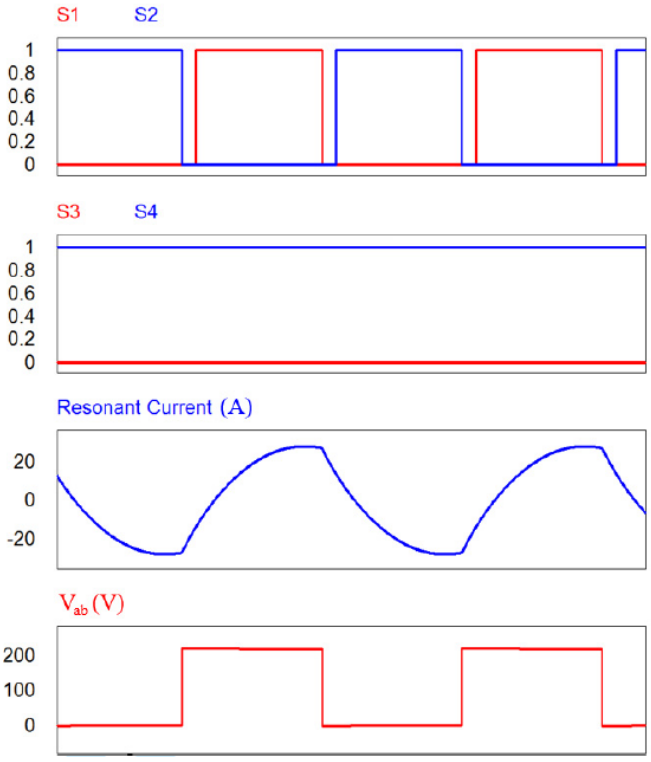

(b)

Fig. 45. Simulation waveforms of input voltage controlling mode: (a) Half-bridge mode, (b) Full-bridge mode

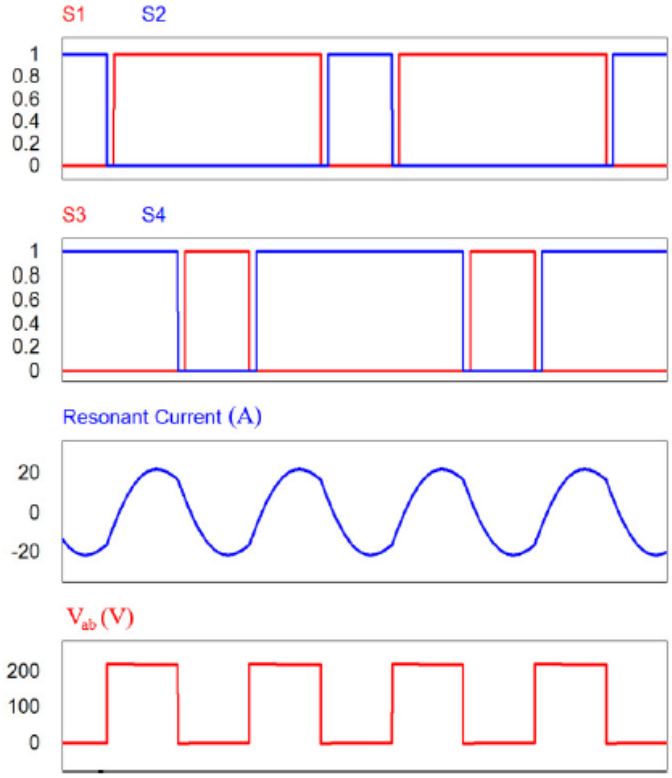

(a)

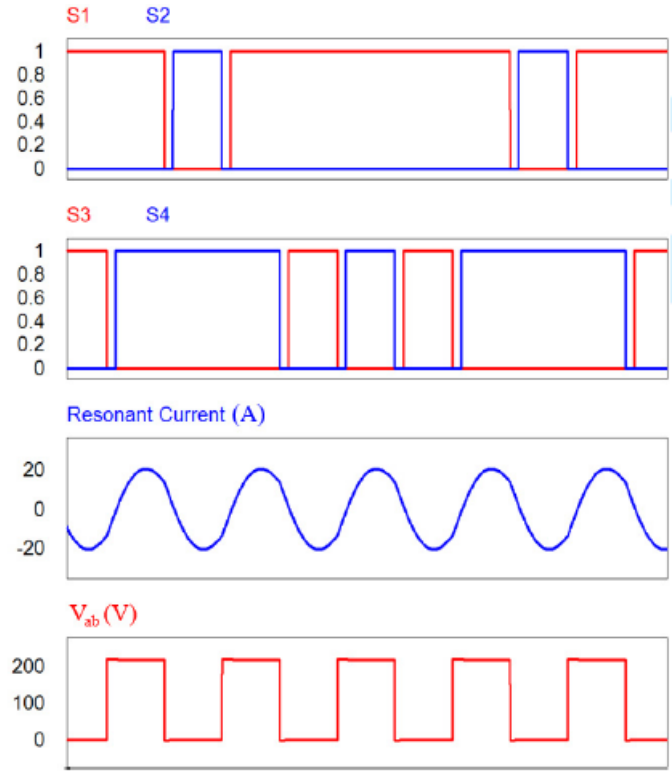

(b)

Fig. 46. Simulation waveforms of operating frequency amplifying mode: (a) Frequency-doubling mode, (b) Frequency-triple mode

TABLE XIII SIMULATION RESULTS OF LAM

SUS-304 18-8 (Full-bridge mode)		Input Voltage, V_i	220 Vdc	Input Current, I_i (RMS)	9.2 A
		Transmission Power, P_o	2.0 kW	Switch current (RMS)	15.3 A
SUS-304 18-10 (Half-bridge mode)		Input Voltage, V_i	220 Vdc	Input Current, I_i (RMS)	9.1 A
		Transmission Power, P_o	2.0 kW	Switch current (RMS)	26.7 A
Aluminum	Frequency Doubler	Input Voltage, V_i	220 Vdc	Input Current, I_i (RMS)	9.2 A
		Transmission Power, P_o	2.0 kW	Switch current (RMS)	26.4 A
	Frequency Tripler	Input Voltage, V_i	220 Vdc	Input Current, I_i (RMS)	9.1 A
		Transmission Power, P_o	2.0 kW	Switch current (RMS)	29.7 A

TABLE XIV EXPERIMENT DESIGN SPECIFICATIONS OF LAM

Transmission Power, P_o		2.0 kW	Resistance of vessel, R_{vessel}	9.65 Ω, at 25 kHz
Input Voltage, V_i		220 Vdc	Resistance of vessel, R_{vessel}	3.16 Ω, at 25 kHz
Turn numbers, N		41 turns	Resistance of vessel, R_{vessel}	2.0 Ω, at 50 kHz
			Resistance of vessel, R_{vessel}	2.2 Ω, at 75 kHz
SUS-304 18-8	Resonant Inductance, L_r	160 uH	Resonant Frequency, f_r	25 kHz
	Resonant Capacitance, C_r	253 nF	Switching Frequency, f_s	28 kHz
SUS-304 18-10	Resonant Inductance, L_r	144 uH	Resonant Frequency, f_r	25 kHz
	Resonant Capacitance, C_r	253 nF	Switching Frequency, f_s	26 kHz
Aluminum	Resonant Inductance, L_r	129 uH	Resonant Frequency, f_r	50 kHz
	Resonant Capacitance, C_r	63.1 nF	Switching Frequency, f_s	52 kHz
Aluminum	Resonant Inductance, L_r	129 uH	Resonant Frequency, f_r	75 kHz
	Resonant Capacitance, C_r	28.1 nF	Switching Frequency, f_s	76.5 kHz

specification. Fig. 45 and Fig. 46 show the simulation waveforms of input voltage controlling mode and simulation waveforms of operating frequency amplifying mode. All the modulation modes are achieved the ZVS operation. As shown in Fig. 45. and Fig. 46, it verifies to control the bridge voltage and operating frequency induced to the IH working coil according to material of pots by changing the modulation modes. TABLE XIII describes the simulation results of the LAM. All the modulation modes achieve the desired power 2 kW within the switch rated current 40 A. The experimental specification is described in TABLE XIV.

Fig. 47 shows the experiment set-up of 2 kW prototype LAM, which has the all-metal IH working coil, power converter, a digital controller (TI TMS320F28335) and AC power supply (KIKUSUI PCR6000LA). Oscilloscope (Teledyenlecroy Waverunner610Zi), and power analyzer (N4L PPA 5530) are used to measure the experimental results. Fig. 48 shows the experimental results of the full-bridge mode. Fig. 49 shows the experimental results of the half-bridge mode. The bridge voltage of the half-bridge mode is two times smaller than the full-bridge mode. Therefore, the full-bridge and half-bridge modes are used to change input voltage. Fig. 50 and Fig. 51 show the experimental results of voltage and current at the frequency-doubling mode and frequency triple mode, respectively. The frequency-

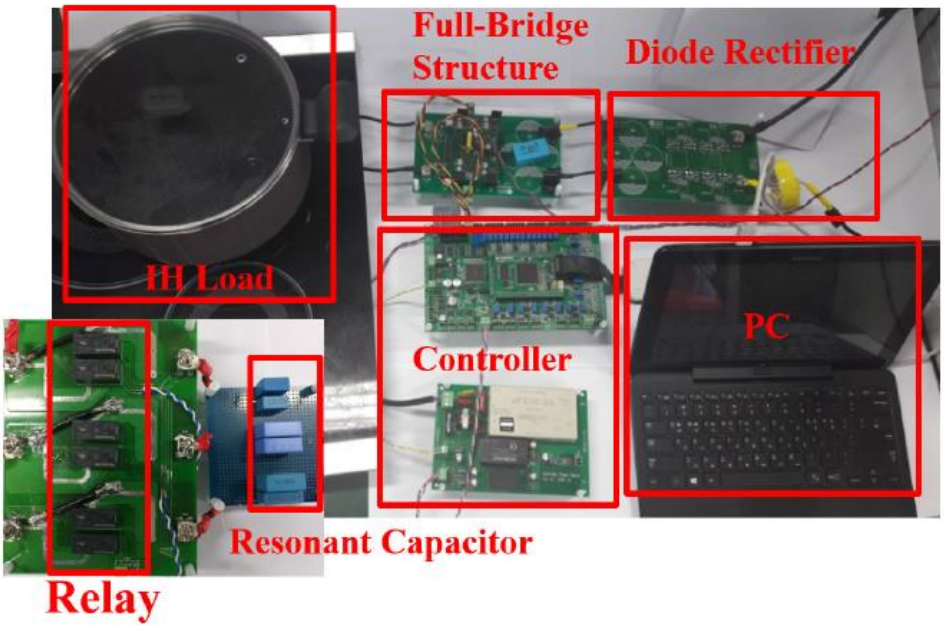

Fig. 47. Experimental setup of 2 kW prototype LAM IH system

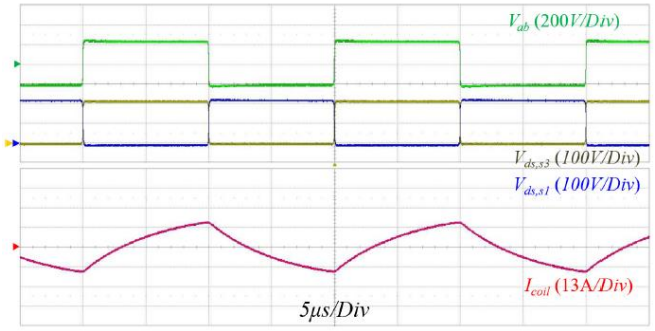

(a)

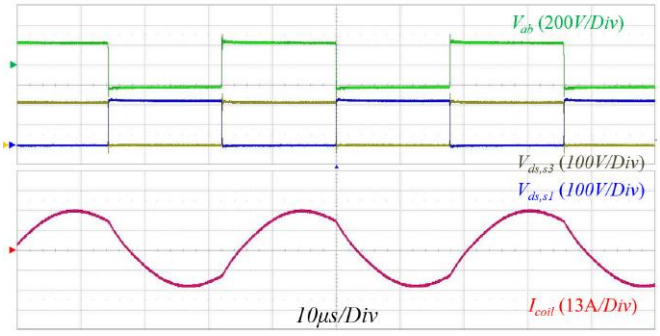

(b)

Fig. 48. Experimental results of full-bridge mode:
(a) 600 W, (b) 2 kW

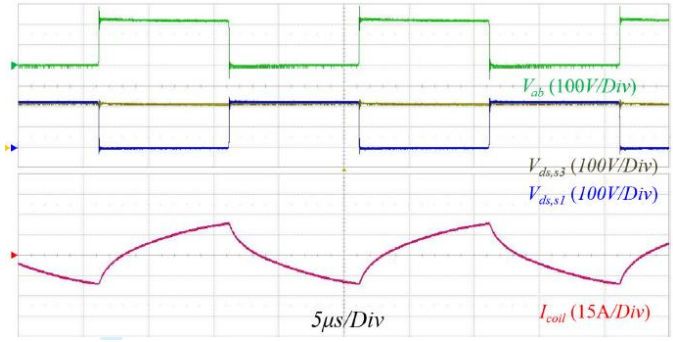

(a)

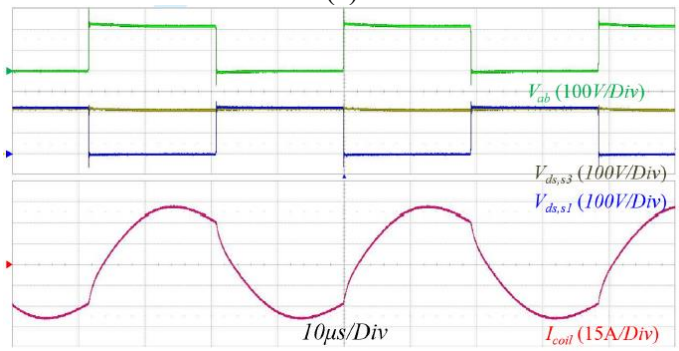

(b)

Fig. 49. Experimental results of half-bridge mode:

(a) 600 W, (b) 2 kW

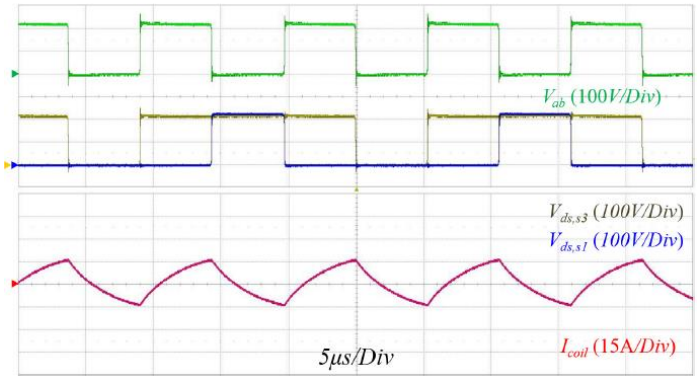

(a)

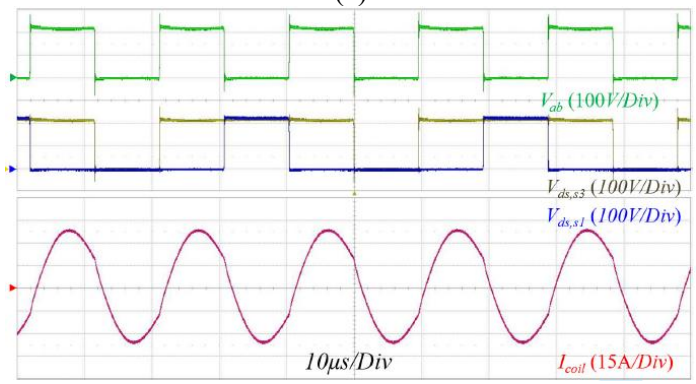

(b)

Fig. 50. Experimental results of frequency-doubling mode:

(a) 600 W, (b) 2 kW

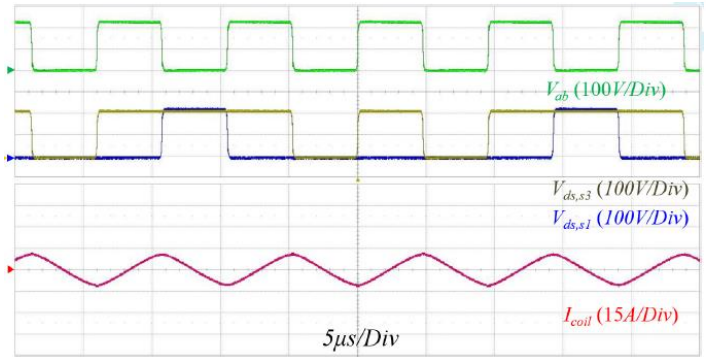

(a)

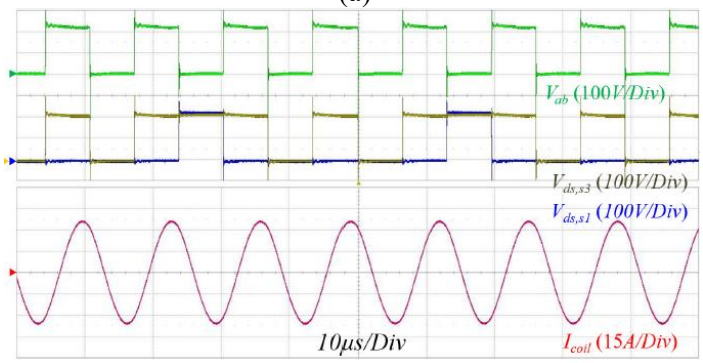

(b)

Fig. 51. Experimental results of frequency-triple mode:
(a) 600 W, (b) 2 kW

doubling and triple modes control the operating frequency induced to the IH working coil in the LAM inverter while increasing switching frequency. Fig. 52 shows the ZVS operation waveforms of the LAM at rated power 2 kW. All the experimental results achieve the ZVS operations, the switch rated current. Fig.53 shows experimental results of the proposed algorithm, which can change modulation modes. It starts from the frequency-triple mode which has the minimum transmission power compared with other modulation modes. After end of the detection of the material, all the switches of the proposed LAM are turned-off, then the relay circuit controls the resonant frequency by changing the resonant capacitor.

TABLE XV describes the experimental results of the LAM. All the proposed modulation modes achieve the rated power 2 kW and satisfy the switch rated current 40 A. Fig. 54 shows the Power efficiency according to the input power. The full-bridge mode of the LAM has the high bridge voltage and the small resonant current, which achieves high efficiency. The half-bridge mode has lower efficiency than the full-bridge mode because the resonant current of the half-bridge mode is higher that of the full-bridge mode. The frequency-doubling mode has the lower resistance than that of the frequency-triple mode because the higher operating frequency induced to the IH working coil induces the larger equivalent load resistance of the load by decreasing skin-depth of the vessel. However,

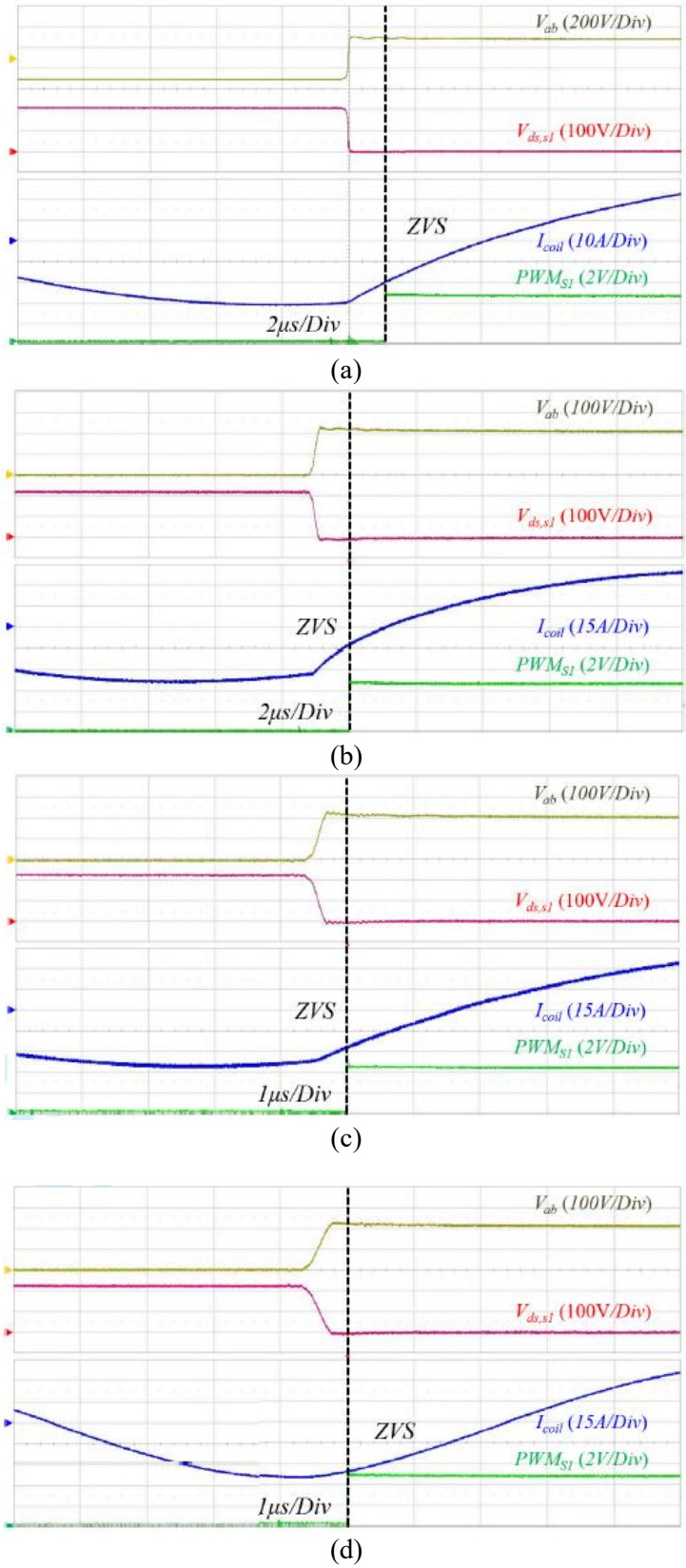

Fig. 52. ZVS operation waveforms of LAM: (a) Full-bridge mode, (b) Half-bridge mode, (c) Frequency-doubling mode, (d) Frequency-triple mode

TABLE XV EXPERIMENTAL RESEULTS OF LAM

SUS-304 18-8 (Full-bridge mode)		Input Voltage, V_i	220 Vdc	Input Current, I_i (RMS)	9.2 A
		Transmission Power, P_o	2.0 kW	Switch current (RMS)	15.3 A
SUS-304 18-10 (Half-bridge mode)		Input Voltage, V_i	220 Vdc	Input Current, I_i (RMS)	9.1 A
		Transmission Power, P_o	2.0 kW	Switch current (RMS)	26.7 A
Aluminum	Frequency Doubler	Input Voltage, V_i	220 Vdc	Input Current, I_i (RMS)	9.2 A
		Transmission Power, P_o	2.0 kW	Switch current (RMS)	26.4 A
	Frequency Tripler	Input Voltage, V_i	220 Vdc	Input Current, I_i (RMS)	9.1 A
		Transmission Power, P_o	2.0 kW	Switch current (RMS)	29.7 A

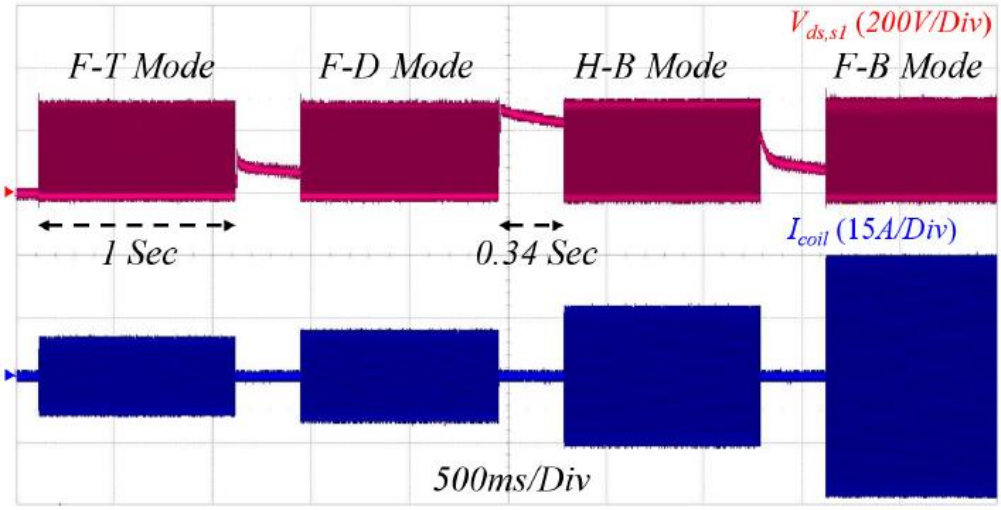

Fig. 53. Experimental result of the proposed algorithm

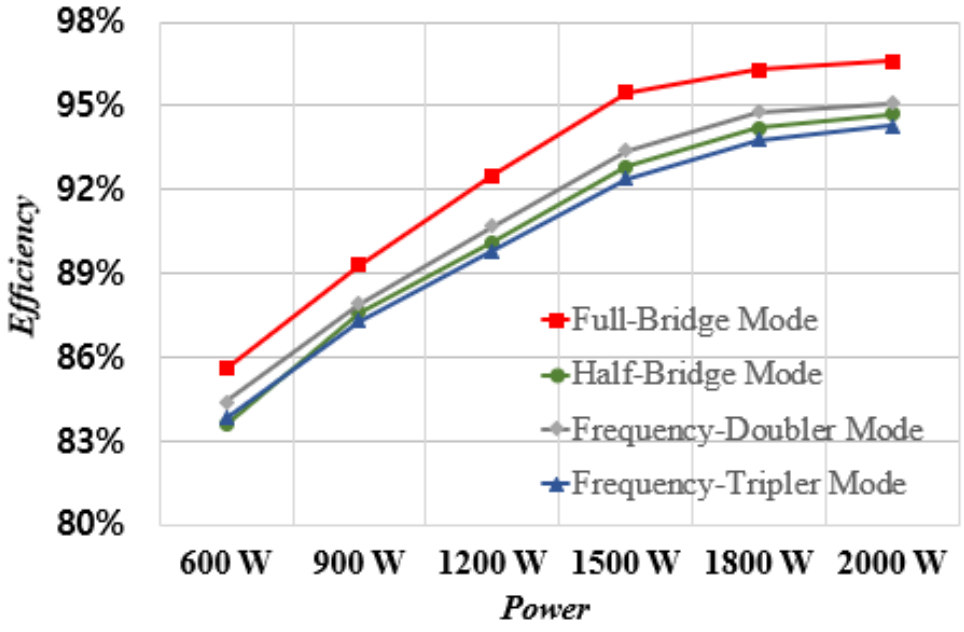

Fig. 54. Power efficiency according to modulation modes

the lagging leg of the frequency-triple mode operates the doubled switching frequency. Therefore, the efficiency of the frequency-triple mode is lower than the frequency-doubling mode.

The switching loss is described in terms of the conduction loss and the switching turn-off loss [37-40]. The switch conduction loss is derived as follows:

$$P_{con,loss} = I_{rms}^2 \cdot R_{ds,on} \tag{26}$$

where $R_{ds,on}$ is the on-resistance and I_{rms} is the switch RMS current. In the full-bridge mode, the switch RMS current for each switch is derived as follows:

$$I_{s1,rms} = I_{s2,rms} = I_{s3,rms} = I_{s4,rms} = \frac{I_{rms}}{2} \tag{27}$$

where $I_{s1,rms}$, $I_{s2,rms}$, $I_{s3,rms}$, and $I_{s4,rms}$ are the rms current of switch 1, 2, 3, and 4, respectively. And I_{rms} is the rums current of the resonant network. For the half-bridge mode, the switch RMS current of each switch is described as follows:

$$I_{s1,rms} = I_{s4,rms} = \frac{I_{rms}}{2} \tag{28}$$

$$I_{s4,rms} = I_{rms} \tag{29}$$

$$I_{s3,rms} = 0 \tag{30}$$

In the frequency-doubling mode, the switch RMS current of each switch is derived as follows:

$$I_{s1,rms} = I_{s4,rms} = \frac{3 \cdot I_{rms}}{4} \tag{31}$$

$$I_{s2,rms} = I_{s3,rms} = \frac{I_{rms}}{4} \tag{32}$$

In the frequency-triple mode, the switch RMS current of each switch is derived as follows:

$$I_{s1,rms} = \frac{5 \cdot I_{rms}}{6} \tag{33}$$

$$I_{s2,rms} = \frac{I_{rms}}{6} \tag{34}$$

$$I_{s3,rms} = \frac{I_{rms}}{3} \tag{35}$$

$$I_{s4,rms} = \frac{2 \cdot I_{rms}}{3} \tag{36}$$

The turn-on loss is negligible because the ZVS operation is achieved under whole modulation modes of the proposed method. The turn-off loss is described as follows:

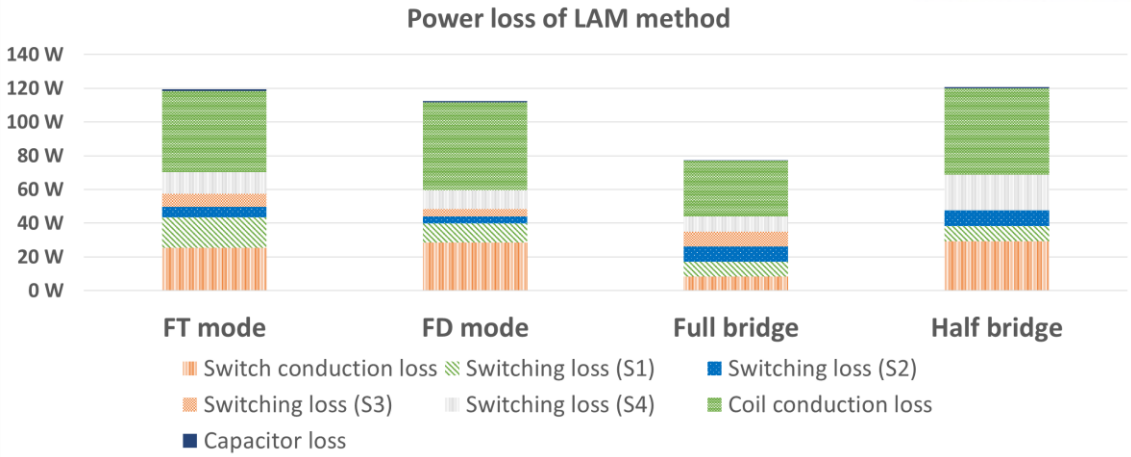

Fig. 55. Power loss according to modulation modes

$$P_{off,loss} \cong \frac{1}{2} \cdot V_{sw} I_{off} t_{off} f_{sw} \tag{37}$$

where V_{sw} is the drain-source voltage, I_{off} is the turn-off current of the power switch, t_{off} is the turn-off time, and f_{sw} is the switching frequency. All the modulation modes except the frequency-triple mode can use (37). The switching loss of all switches is same. However, the frequency-triple mode has different switching loss for each switch. It is described as follows:

$$P_{s1,off,loss} = P_{s1,off,loss} = P_{off,loss} \tag{38}$$

$$P_{s3,off,loss} = P_{s4,off,loss} = 2 \cdot P_{off,loss} \tag{39}$$

The loss analysis according to the modulation modes at the rated power 2 kW are shown in Fig. 55. In the frequency-triple mode, the lagging leg switches are operated as the doubled switching frequency. It induces the high switching loss. At the half-bridge mode, the switch S4 is always turn-on which induces the high switching loss.

Conclusions

The design methodology and performance evaluation of a LAM is analyzed by using PSIM simulation and the 2 kW experimental prototype. In this paper, the LAM is proposed to solve a cost issue of the all-metal IH technology and obtain the heating capability for the ferro- and non-ferromagnetic materials. The LAM solves the cost issue of the conventional all-metal induction heating technologies such as HFO and THM methods. The HFO method uses SiC devices to decrease the high switch heat which is induced by operating the high switching frequency. And the THM methods uses the front-end active PFC to compensate the voltage gain drop which is induced by operating the resonant network as the third harmonic filter. The LAM implements the all-metal IH technology using only a full-bridge structure.

The proposed modulation modes of the LAM use a zero-vector to increase the operating frequency induced to the IH working coil without increasing the switching frequency. The zero-vector of the proposed modulation modes increases the frequency of the bridge square wave voltage by dividing the switching period. The amplified operating frequency increases the effective resistance of the non-ferromagnetic material by reducing its skin-depth. It solves the high switch heat generated by operating the high switching frequency, or the voltage gain drop due to a third harmonic operation. And the proposed modulation modes can change the input voltage magnitude. The half-bridge and full-bridge mode change the equivalent input voltage. It is possible to heat both the low resistance ferromagnetic material and the high resistance ferromagnetic material by controlling the input voltage which is controlled by changing modulation modes. The frequency-doubling and the frequency-triple modes can change the operating frequency induced to the IH working coil. These two modes are selected to heat the desired power by controlling the operating frequency induced to the IH working coil.

In this paper, the operational principle of the LAM, the LAM algorithm, the design methodology, and the performance evaluation are analyzed. The simulation and experimental results with the 2 kW all-metal IH inverter verifies how the proposed SRC IH inverter successfully heats the vessels made from ferromagnetic and non-ferromagnetic material. In addition, it verified the heating performance of non-ferromagnetic and ferromagnetic material without the active PFC, soling the cost problem of the conventional all-metal IH technologies.

REFERENCES

1. S. M. Park, H. G. Woo, and D. C. Shin, "A study on the stabilization of induction heating system for using high-frequency series resonant inverter," 2010 Power Electronics Annual Conference, pp. 506-507, Jul. 2010.

2. Oscar Lucia, and Pascal Maussion, "Induction heating technology and its applications: past developments, current technology, and future challenges",2014 IEEE TRANSACTIONS ON INDUSTRIAL ELECTRONICS, pp. 2509-2520, May. 2014.

3. Rajaram.M.K. and Booma.N, "Resonant inverter for induction heating",2012 International conference on computing, electronics and electrical technologies [ICCEET], pp. 358-366, May. 2012.

4. Nistor Daniel Trip, Adrian Burca, Teodor Leuca, and Jaroslav Dudrik, "Considerations on the analysis of an induction heating system", 2014 11th International Symposium on Electronics and Telecommunications (ISETC), Nov. 2014.

5. Adrian Burca ; Nistor Daniel Trip ; Teodor Leuca, "Considerations on the design of a low power induction heating system", 2014 International Symposium on Fundamentals of Electrical Engineering (ISFEE), Nov. 2014.

6. Tsvetozar and Stalmir, "Investigation of Two Parallel Converters for Induction Heating, Supplying a Common Load", 2018 IX National Conference with International Participation (ELECTRONICA), May 2018.

7. Hiroki Shinagawa, Takayuki Suzuki, and Masahiro Noda, "Theoretical Analysis of AC Resistance in Coil Using Magnetoplated Wire", IEEE Transactions on Magnetics, Aug. 2009.

8. R.K. Barton, "Eddy current and skin effect in edgewise wound copper coils", IEEE Transactions on Magnetics", July. 1989.

9. Mahdi Hediehloo and Mahdi Akhbari, "New approach in design of planar coil of induction cooker based on skin and proximity effects analysis", 2009 IEEE International Conference on Industrial Technology, Feb. 2009.

10. I. Millan, D. Puyal, J.M. Burdio, J. Acero, and Sergio Llorente, "Resonant Inverter Topology for All-metal Domestic Induction Heating", 2007 IEEE International Symposium on Industrial Electronics, June. 2007.

11. Millan, J.M. Burdio, and J.Acero, "Series resonant inverter with selective harmonic operation applied to all-meatl domestic induction heating", IET Power Electronics, Mar. 2010.

12. Takayuki Hirokawa, Eiji Hiraki, Toshihiko Tanaka, Masayuki Okamoto, and Mutsuo Nakaoka, "The Practical Evaluations of Time-Sharing High-Frequency Resoantn Soft-Switching Inverter for All Metal IH Cooking Appliances, 2012 IEEE International Conference on Industrial Technology, Mar. 2012.

13. Mario Pérez-Tarragona, Héctor Sarnago, Óscar Lucía, and José M. Burdío, "Full-bridge series resonant multi-inverter featuring new 900-V SiC devices for improved induction

heating appliances", 2016 IEEE Applied Power Electronics Conference and Exposition (APEC), May. 2016.

14. Sang-Min Park, Eun-Su Jang, Dong-Myoung Joo, Byoung-Kuk Lee, "Design of Control System for All-Metal Domestic Induction Heating Considering Temperature and Quick-Response", THE KOREAN INSTITUTE OF POWER ELECTRONICS, Feb.2016.

15. P. Achara, P. Viriya, and K. Matsuse, "Analysis of a Half - Bridge Inverter for a Small-Size Induction Cooker Using Positive-Negative Phase-Shift Control under ZVS and NON-ZVS Operation", 2007 7th International Conference on Power Electronics and Drive Systems, Apr. 2008.

16. Li Jin ; Bangyin Liu, Shanxu Duan, "ZVS operation range analysis of three-level dual active bridge DC-DC converter with phase-shift control", 2017 IEEE Applied Power Electronics Conference and Exposition (APEC), May. 2017.

17. Xiuqin Wei, Hiroo Sekiya, and Tadashi Suetsugu, "A novel approach for achieving ZVS operation in class-D ZVS inverter", 2017 IEEE 12th International Conference on Power Electronics and Drive Systems (PEDS), Dec. 2017.

18. Jing Xue, Hoi Lee, "A 2 MHz 12–100 V 90% Efficiency Self-Balancing ZVS Reconfigurable Three-Level DC-DC Regulator With Constant-Frequency Adaptive-On-Time V2 Control and Nanosecond-Scale ZVS Turn-On Delay", IEEE Journal of Solid-State Circuits, Sep. 2016.

19. Li Jin, Bangyin Liu, and Shanxu Duan, "ZVS Soft Switching Operation Range Analysis of Three-Level Dual Active Bridge DC-DC Converter under Phase Shift Control Strategy", IEEE Transactions on Industry Applications, Sep. 2018.

20. Xiaoming Zhang, Tao Cai, Shanxu Duan, Hao Feng, Hongsheng Hu, and Jintao Niu, "A Control Strategy for Efficiency Optimization and Wide ZVS Operation Range in Bidirectional Inductive Power Transfer System", IEEE Transactions on Industrial Electronics", Sep. 2018.

21. Robert L, Steigerwald, "A Comparison of Half-Bridge Resonant Converter Topologies", IEEE Transactions of Power Electronics, vol 3, no. 2, Apr. 1988.

22. Wei Han, K. T. Chau, Chaoqiang Jiang, and Wei Liu, "All-Metal Domestic Induction Heating Using Single-Frequency Double-Layer Coils", IEEE Transactions on Magnetics, June. 2018.

23. D Mounika, S Porpandiselvi, and V K Satyakar Veeramallu, "Dual frequency full-bridge inverter for all metal induction heating cooking applications", 2017 International Conference on Inventive Computing and Informatics (ICICI), May. 2018.

24. I. Millan, D. Puyal, J.M. Burdio, J. Acero, and Sergio Llorente, "Resonant Inverter Topology for All-Metal Domestic Induction Heating", 2007 IEEE International Symposium on Industrial Electronics, June. 2007.

25. Takayuki Hirokawa, Eiji Hiraki, Toshihiko Tanaka, Makoto Imai, and Kenji Yasui, "Dual-frequency multiple-output resonant soft-switching inverter for induction heating cooking appliances", IECON 2013 - 39th Annual Conference of the IEEE Industrial Electronics Society, Nov. 2013.

26. Enrique J. Dede, José Jordán, and Vicente Esteve, “The practical use of SiC devices in high power, high frequency inverters for industrial induction heating applications”, 2016 IEEE 2nd Annual Southern Power Electronics Conference (SPEC), Feb. 2017.

27. Dianbo Fu, “Topology Investigatin and System Optimization of Resonant Converter”, Doctor of Philosophy in Electrical Engineering, Dessertation submitted to the Faculty of the Virginia Polytechnic Institute and State University, Feb. 2010.

28. Andrew Aloysius Amrhein, “Induction Heating of Aluminum Cookware”, Thesis submitted to the faculty of the Virginia Polytechnic Institute and State University in partial fulfillment of the requirements of the degree of Master of Sience In Electrical Engineering, May. 2015.

29. Erdal Gonendik, “High Efficiency Arrays of Inductive Coils”, M.S. in Electrical and Electronics Engineering and the Graduate School of Engineering and Science of Bilkent University, July. 2014

30. Veeramraju T. Somasekhar, Srirama Srinivas, and Kommuru Kranti Kumar, “Effect of Zero-Vector Placement in a Dual-Inverter Fed Open-End Winding Induction-Motor Drive With a Decoupled Space-Vector PWM Strategy”, IEEE Transactions on Industrial Electronics, May. 2008.

31. Kaimin Shi, Donglai Zhang, Zhicheng Zhou, Mengqiao Zhang, and Yu Gu, “A Novel Phase-Shift Dual Full-Bridge Converter With Full Soft-Switching Range and Wide Conversion Range”, IEEE Transactions on Power Electronics, Dec. 2015.

32. Oladimeji Ibrahim, Nor Zaihar Yahaya, Nordin Saad, and K. Y. Ahmed, “Design and simulation of phase-shifted full bridge converter for hybrid energy systems”, 2016 6th International Conference on Intelligent and Advanced Systems (ICIAS), Aug. 2016.

33. Yu-Kang Lo, Chung-Yi Lin, Min-Tsong Hsieh, and Chien-Yu Lin, “Phase-Shifted Full-Bridge Series-Resonant DC-DC Converters for Wide Load Variations”, IEEE Transactions on Industrial Electronics, July. 2010.

34. Junichi Yamamoto, Toshiyuki Zaitsu, Seiya Abe, and Tamotsu Ninomiya, “PFM and PWM Hybrid controlled LLC converter”, 2014 International Power Electronics Conference (IPEC-Hiroshima 2014 - ECCE ASIA), Aug. 2014.

35. Junkai Zhao, Herbert H.C. Iu, and Tyrone Fernando, “The design of cascaded DC-DC converters with single-switch PWM and PFM for standalone PV power applications”, 2017 IEEE 3rd International Future Energy Electronics Conference and ECCE Asia (IFEEC 2017 - ECCE Asia), July. 2017.

36. K. I. Hwu, and Y. T. Yau, “Improvement of one-comparator counter-based PFM control for DC-DC converter”, 2009 IEEE International Symposium on Industrial Electronics, July. 2009.

37. C. Oeder, M. Barwig, and T. Duerbaum, “Estimation of switching losses in resonant converters based on datasheet information”, 2016 18th European Conference on Power Electronics and Applications (EPE'16 ECCE Europe), Sept. 2016.

38. M. Ghasem HosseinI Aghdam, S.H. Fathi, and A. Ghasemi, “The Analysis of Conduction and Switching Losses in Three-Phase OHSW Multilevel Inverter Using Switching Functions”,

2005 International Conference on Power Electronics and Drives Systems, April. 2006.

39. Anup Anurag, Sayan Acharya, Yos Prabowo, and Ghanshyamsinh Gohil, “An accurate calorimetric method for measurement of switching losses in silicon carbide (SiC) MOSFETs”, 2018 IEEE Applied Power Electronics Conference and Exposition (APEC), April. 2018.

40. Keiji Wada, and Masato Ando, “Switching Loss Analysis of SiC-MOSFET based on Stray Inductance Scaling”, 2018 International Power Electronics Conference (IPEC-Niigata 2018 -ECCE Asia), May. 2018.